Turbulent mixing in Barrow Strait

Greg Crawford[a,1], Laurie Padman[b,*], Miles McPhee[c]

[a] *College of Oceanic and Atmospheric Sciences, Oregon State University, Corvallis, OR 97331-5503, USA*
[b] *Earth and Space Research, 1910 Fairview Ave. E., Suite 102, Seattle, WA 98102-3620, USA*
[c] *McPhee Research Company, 450 Clover Springs Road, Naches, WA 98937, USA*

Abstract

Data collected in Barrow Strait during April and May 1995 indicate that turbulence can occur throughout the water column, with the most energetic turbulence being associated with strong currents during spring tides. In the surface mixed layer (SML) under the first-year, land-fast ice, the average effective vertical diffusivity was proportional to current speed, with mean values ranging up to $0.02 \, \text{m}^2 \, \text{s}^{-1}$. Current speeds in the SML during tidal maxima sometimes exceeded $20 \, \text{cm} \, \text{s}^{-1}$ but turbulent stress levels remained low because the ice under-surface was hydrodynamically smooth. An asymmetry observed in undersurface drag during the tidal cycle is associated with changes in eddy viscosity, possibly in response to the advection of a horizontal salinity gradient in the SML in this region. In the sharp halocline ($N \approx 15\text{–}20$ cycles h^{-1}) at the base of the SML, mixing was often too weak to transport heat, salt, and other scalars vertically. During such periods the halocline acts as a barrier to the transport of properties, such as nutrients, from the deeper water to the surface. Within the deeper, less-stratified, water ($N \approx 3\text{–}5$ cycles h^{-1}), energetic mixing frequently occurred, and was modulated by both the spring/neap tidal variability and within each tidal cycle. The water column was, on average, fresher than observed in previous spring measurements from this area, suggesting interannual variability in the Archipelago hydrography. © 1999 Elsevier Science Ltd. All rights reserved.

1. Introduction

The complex network of passages through the Canadian Arctic Archipelago (Fig. 1) is an important pathway for mass and heat exchange between the upper layers of the western Arctic Ocean and the North Atlantic Ocean via Baffin Bay (Rudels, 1986;

** Corresponding author. Tel.: 001 206 726 0501; fax: 001 206 726 0524; e-mail: padman@esr.org.

[1] Present address: Department of Oceanography, Humboldt State University, Arcata, CA 95521-8299, USA.
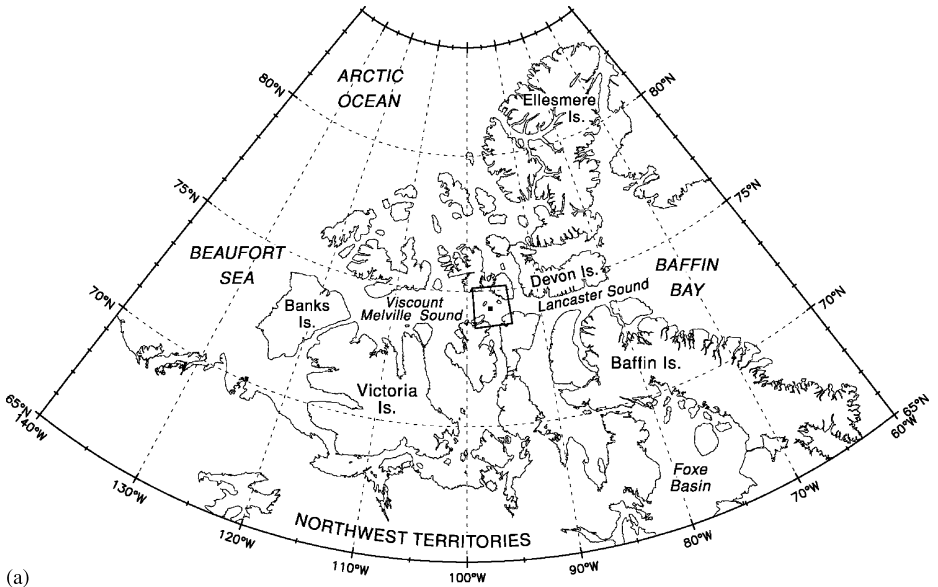
(a)
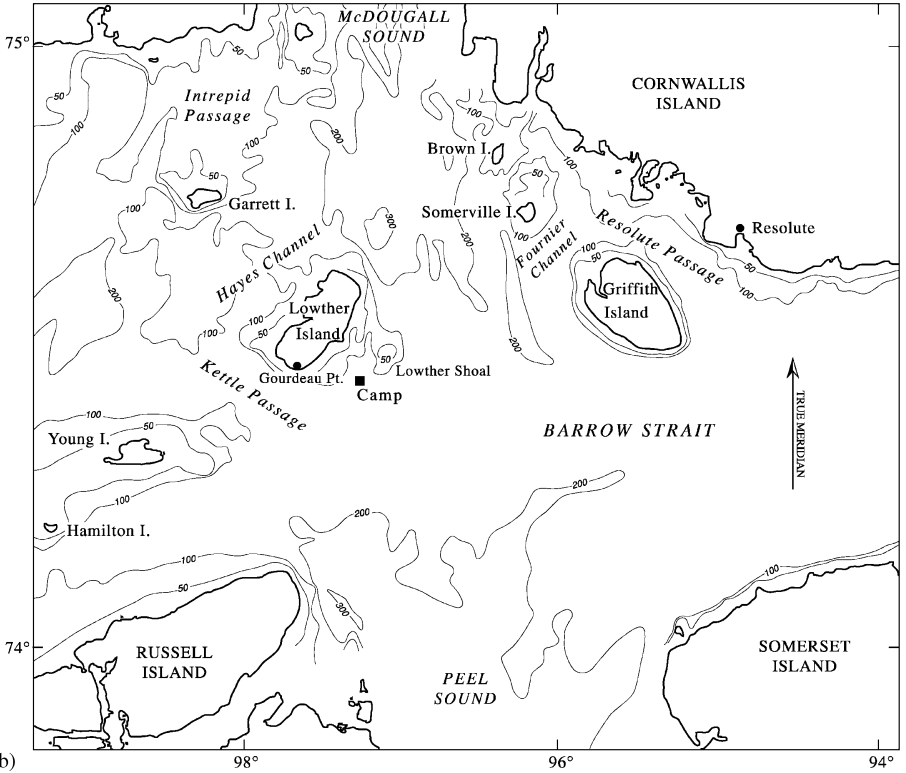
(b)

Fissel et al., 1988; Steele et al., 1996). Shallow sills prevent the direct advective transport of deep water through the Archipelago (Melling et al., 1984), therefore lateral fluxes of the properties of the deeper water types require that one or more mechanisms be present to transport the properties vertically through the water column. Effective mechanisms include diapycnal mixing and stirring along sloping isopycnals.

In April and May 1995, a measurement program (denoted herein as RES95) was carried out from the land-fast ice in Barrow Strait (Fig. 1b) to investigate the physical processes that are responsible for diapycnal mixing. Candidate processes include instabilities initiated by the vertical gradient of horizontal velocity, advective instabilities associated with large-amplitude internal waves and solitons, and boundary-layer influences at the seabed and at the base of the land-fast ice. Additional data were obtained to explore the vertical fluxes through the nearly neutral stratification of the surface mixed layer ('SML').

Tidal currents are large in several regions of the Archipelago (Stronach et al., 1987; Prinsenberg and Bennett, 1989a, b; Kowalik and Proshutinsky, 1994; Lyard, 1997), and provide energy for boundary mixing and generation of internal gravity waves (including baroclinic tides). Large-amplitude internal waves and solitons (non-linear internal wave packets) have also been observed, and an association between them and the hydrographic signature of mixing (i.e., density inversions) has been noted (Marsden et al., 1994a, b). These waves appear to derive their energy from tidal currents, since they are most frequently observed during periods of spring tides. Tide-generated internal gravity waves (including baroclinic tides) are found in numerous regions of the world, near and over shelves and continental slopes where tidal currents are significant and the stratification supports their generation (e.g., Baines, 1986).

The unique aspect of RES95 relative to prior studies of mixing in the Archipelago is our direct measurement of turbulence levels in both the SML and the deeper stratified water column. In this paper we first describe the relevant components of the RES95 program (Section 2), then briefly review methods for determining diapycnal diffusivities and the associated scalar fluxes (Section 3). Hydrographic conditions, internal wave properties, and mixing rates in the various regimes that were sampled in RES95 are described in Section 4. The implications of these measurements for modeling of the regional hydrography and circulation are discussed (Section 5), and our findings are summarized in Section 6.

Fig. 1. (a) Map of the Canadian Archipelago, showing the major water bodies and islands. The study area is in the marked area in Barrow Strait, in the central Archipelago between Viscount Melville Sound and Lancaster Sound. (b) Expanded view of the study area, showing the location of the RES95 camp (74°27.398′ N, 97°15.788′ W), about 8 km southeast of Lowther Island, in Barrow Strait. Bathymetric contours are in meters.

2. The RES95 program

2.1. Overview

RES95 was a physical oceanographic measurement program carried out by R. Marsden (Royal Roads Military College), G. Ingram (McGill University), L. Padman (Oregon State University), and M. McPhee (McPhee Research Company). Glenn Cota (University of Tennessee) obtained biological and nutrient properties within and under the sea ice for roughly the same period. The ice camp was established about 8 km southeast of Lowther Island (Figs. 1b and 2) on smooth, first-year, land-fast ice about 1.8 m thick. Thicker and much rougher multi-year ice was present along the coast of Lowther Island and over Lowther Shoals, northeast of the camp. The highly variable distribution of ice cover characteristics indicated in Fig. 2 is expected to play a significant role in upper ocean mixing in this region.

The camp layout is shown in Fig. 3. The water depth at this site was about 160 m, varying by a few meters across the camp. The instruments, in particular the three acoustic Doppler current profilers (ADCPs), were arranged to measure the directional properties of high-frequency internal waves. The spacing of the ADCPs (150–200 m) was chosen as a reasonable fraction of the expected wavelengths of these waves, which in previous studies were about 1 km (Marsden et al., 1994a, b). The microstructure profiler was deployed near the 317 kHz ADCP in the main science hut, so that we recorded the velocity shear field that was most relevant to the observed microstructure. In this paper we will focus on data from the microstructure profiler, the mixed layer turbulence frame, the ADCP mounted in the main science hut, and the temperature-conductivity mooring. These systems are described in the following subsections. Future work will address the information available from the ADCP spatial array.

2.2. Microstructure profiling

We collected about 1200 microstructure profiles using the Rapid-Sampling Vertical Profiler (RSVP) (Caldwell et al., 1985; Robertson et al., 1995) between 25 April and 17 May 1995. These dates correspond to day-of-year (DOY) 115 to 137. Throughout this paper, time t will be given in decimal day-of-year 1995 (UT), where $t = 1.0$ is 0000 UT on January 1. Most profiles extend from the surface to a depth of about 110 m, about 45 m from the seabed. Because of limited personnel and our assessment that most mixing was expected to be related to tides, we performed profiling continuously for two periods of the dominant M_2 tide (about 25 h total), followed by 23 h with no profiling, for a repeat interval of 2 d. Nine 'batches' of approximately 100 profiles per batch were obtained in this manner from DOY 120 to 137 (Table 1). This sampling covered one complete spring/neap cycle, with temporal resolution during each batch of about four profiles per hour.

The RSVP is a tethered, free-fall profiler about 1.3 m long. Sensors for measuring temperature (T), conductivity (C), pressure (P), and microscale velocity shear ($u_Z = \partial u / \partial z$ and $v_Z = \partial v / \partial z$) are located on the profiler's nose. Each data channel was
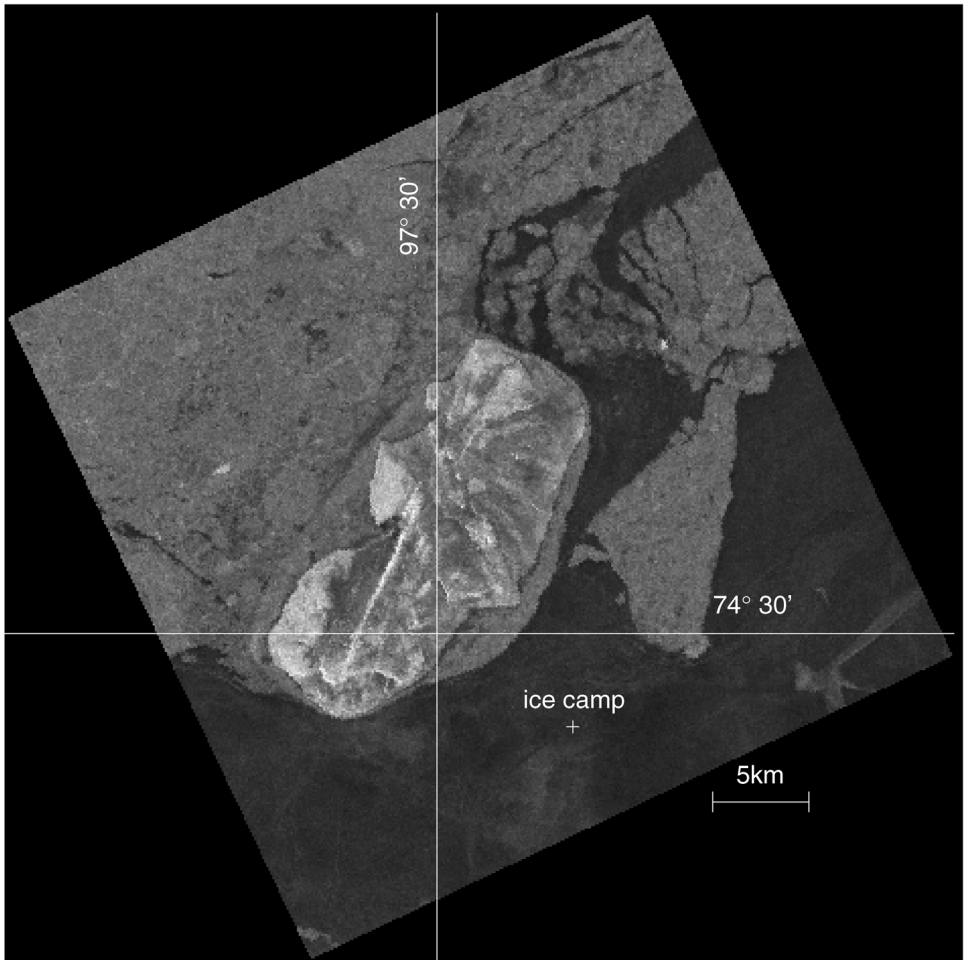
Fig. 2. A portion of a SAR image (uncalibrated backscatter intensity) obtained by the ERS-1 satellite on 2 May 1995 (year day 122). The image has been rotated so that the top of the page is north. Pixel resolution is roughly 100 m. Lowther Island is clearly identifiable. The ice camp (' + ') was established on smooth, land-fast first-year ice about 8 km southeast of Lowther Island. The medium-gray masses along the coast of Lowther Island and to the northeast of the study site represent land-fast, multi-year ice.
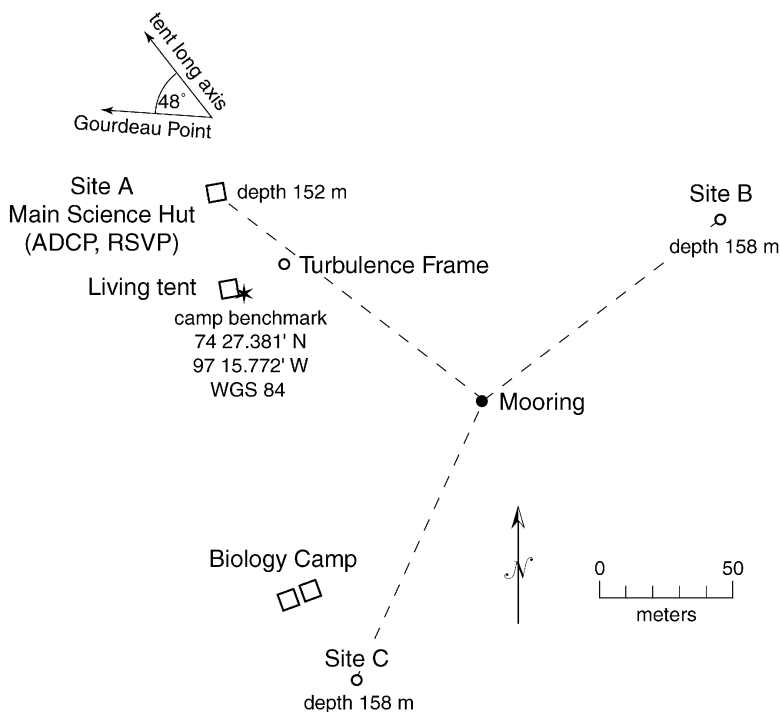
.

Fig. 3. A plan map of the ice camp, showing locations of primary instrumented sites. The 317 kHz ADCP and the microstructure profiler were both deployed from Site A (upper left). Moored sensors were deployed from the 'Mooring' site in the center of the camp. Surface layer turbulence measurements were made from the 'Turbulence Frame' site, between Site A and the Mooring. Additional ADCPs were deployed at sites B and C by R. Marsden (Royal Military College, Canada) and G. Ingram (McGill University, Canada), respectively.

sampled at 256 Hz. The fall rate was about $1.2 \, \text{m s}^{-1}$; therefore, each profile to 110 m required less than two minutes. A Thermometrics FP07 thermistor and a Neil Brown Instruments Systems microconductivity cell were used to measure T and C, respectively. These sensors were calibrated against daily-averaged measurements from moored sensors (see Section 2.5, below). Least significant bit (*lsb*) resolutions of the raw 16-bit records are about $1.5 \times 10^{-5}\,^\circ\text{C}$ in T and $7 \times 10^{-5} \, \text{mS cm}^{-1}$ for C. Typical *rms* noise levels based on measurements in non-turbulent mixed layers are about an order of magnitude greater than the *lsb* resolution in T ($10^{-4}\,^\circ\text{C}$) and in C (5×10^{-4} mS cm^{-1}). Salinity 'spiking' due to the mismatch between the time constants and locations of the T and C sensors is well known (e.g., Robertson et al., 1995), but the temperature structure in this region is so weak that the mismatch plays an insignificant role in the determination of salinity (S) and potential density (σ_θ). Profiles of T and C averaged over 1 s (256 points) were used to generate values of S and σ_θ at approximately 1.2 m depth intervals. Temperatures were converted to potential temperature (θ) using S and P.

Table 1
Details of the nine batches of RSVP microstructure profiles, including: the time of first and last profiles in each batch; the total number of profiles; the mean depth of the center of the halocline, $\langle z_h \rangle$; the standard deviation of the depth of the center of the halocline, $\sigma_{z,h}$; and the average maximum buoyancy frequency in the halocline, $N_{\max}$. The standard deviation of the current velocity at 13 m, σ_{U13}, is also shown as a guide to the phase of the spring/neap tidal cycle

Batch number	Time range	Number of drops	$\langle z_h \rangle$ (m)	$\sigma_{z,h}$ (m)	$N_{\max}$ (cph)	σ_{U13} (m s^{-1})	Comments
1	120.47–121.71	122	11.0	4.0	14	0.08	
2	122.63–123.67	101	11.4	4.2	14	0.11	Minor spring
3	124.99–126.05	89	9.4	3.1	13.5	0.11	
4	126.62–127.67	113	8.9	2.8	14.6	0.08	
5	128.62–129.67	110	10.2	2.4	14.2	0.06	Neap
6	130.04–131.08	102	9.8	1.2	16.0	0.06	Neap
7	132.54–133.73	109	9.8	1.6	17.4	0.07	
8	134.45–135.52	107	9.6	2.7	17.3	0.10	
9	136.49–137.52	141	13.7	4.1	15.6	0.12	Major spring

Two airfoil shear sensors were mounted orthogonally on the RSVP to measure u_z and v_z, although one probe failed very early during the experiment. These probes have a spatial resolution of approximately 0.03 m (Osborn and Crawford, 1980) and can, therefore, resolve most of the Kolmogorov shear spectrum (Tennekes and Lumley, 1987) for typical oceanic turbulence levels. The dissipation rate of turbulent kinetic energy (ε) was calculated from the shear spectra by

$$\varepsilon = \frac{15}{2} \, v \int_0^\infty \varphi(k_z) \, dk_z \qquad (1)$$

where v is the kinematic viscosity of seawater ($v \approx 1.85 \times 10^{-6}$ m^2 s^{-1} for these temperatures and salinities), $\varphi(k_z)$ is the power spectrum of measured shear for one velocity shear component (u_z), and k_z is the vertical wave number. The factor 15/2 results from assuming that the velocity fluctuations are isotropic (Tennekes and Lumley, 1987). This assumption is generally valid when ε is sufficiently large that the buoyancy or 'Ozmidov' length scale, $L_b = (\varepsilon/N^3)^{1/2}$, is much greater than the viscous or 'Kolmogorov' scale, $L_k = (v^3/\varepsilon)^{1/4}$ (Dillon, 1984). The ratio of these length scales can be written in terms of an 'activity' index,

$$A_T = \varepsilon/vN^2. \qquad (2)$$

If A_T is greater than about 24, then most velocity shear variance will be found at spatial scales that are unaffected by buoyancy or molecular viscosity (i.e., the 'inertial subrange') (Stillinger et al., 1983). If A_T is much smaller than 24, buoyancy forces and viscosity prevent the turbulence from efficiently transporting fluid scalar properties across the diapycnal property gradients.

In practice, u_z is measured over a finite wave number range, set by a number of constraints including the shear probe's spatial resolution, instrument and electronic

noise levels, and the profiler's coupling to low wave number current variations. The smallest averaging interval used in the present study was 1 s, or about 1.2 vertical meters. Prior to calculating ε, the velocity shear records were edited for obvious spikes resulting from anomalous fall speeds or encounters with biota. Additionally, shear values greater than 3 standard deviations from the mean shear for each 1 s interval were excluded from the variance calculations, since the majority of these large shears were believed to be related to biota impacts or electronic noise. Dissipation rates were then calculated from the shear spectrum using an iterative integration algorithm designed to reduce contamination by broadband instrument noise; details of this algorithm are provided by Crawford and Padman (1997). For ε above the noise floor of $\varepsilon_n \approx 2 \times 10^{-9}$ m^2 s^{-3}, the despiking based on standard deviation usually made little difference to estimates of ε.

2.3. Mixed layer turbulence mast

Continuous turbulence measurements were made at four levels in the upper part of the water column at the RES95 site using Turbulence Instrument Clusters (TICs) mounted 3 m apart on a rigid mast suspended through a hole in the ice. Each TIC comprises three partially ducted rotor current meters oriented along orthogonal axes (two of which are tilted 45° from horizontal), which are mounted near fast-response thermistors and ducted conductivity meters (McPhee and Smith, 1976). If observations are made in a 'mixed layer' where stratification is weak enough to allow a developed inertial subrange in the turbulence spectra, each cluster measures u, v, and w velocity components along with temperature fluctuations at scales small enough to resolve turbulence fluxes directly. That is, the TIC captures most of the zero-lag covariance between vertical velocity, and horizontal velocity and temperature (McPhee, 1992, 1994; McPhee and Stanton, 1996).

The mast was positioned so that the topmost cluster (TIC-1) was 2 m below the ice–water interface. The system requires fairly stringent alignment into the mean flow so that all three mechanical current meters on each cluster sense enough of the flow to remain above a threshold velocity of 1–2 cm s^{-1}. This was accomplished by installing a direction vane between TIC-1 and TIC-2 (2 and 5 m below the ice), which maintained their orientation fairly well. We found, however, that the lower two clusters (8 and 11 m below the ice) were often within the pycnocline below the mixed layer, and that the angular current shear between the mixed layer and pycnocline was often large enough to cause threshold problems in at least one velocity component. There was also much stronger stratification and internal wave activity at the lower depths, adding to the difficulty of estimating Reynolds fluxes. We thus concentrate here on the upper two clusters only. The compass normally used to determine flow direction with the TIC mast was unreliable in the weak horizontal magnetic field of the region: absolute flow direction was, therefore, determined by comparison with the rigidly mounted acoustic Doppler current meter (see Section 2.4, below).

Data from each TIC were grouped into 15 min 'flow realizations', which represent (by Taylor's hypothesis) approximations to instantaneous flow ensembles characterizing the turbulence fields. The realizations were screened to include only segments for

which all three current meters were non-zero at least 90% of the time. For the period from DOY 117 to 138, there was 171 h (33% of total time) and 213 h (42%) of usable data for TIC-1 and TIC-2, respectively. For each flow realization, the velocity components were rotated into a reference frame with zero mean vertical velocity, and the u component aligned with the mean flow vector. Zero-lag covariances were then used to calculate local kinematic Reynolds stress ($\langle u'w'\rangle + i\langle v'w'\rangle$) and turbulent heat flux ($\rho c_p \langle w'T'\rangle$), where primes indicate deviation from the ensemble mean, ρ is density, and c_p is the specific heat. We define the scalar friction velocity as $u_*(z) = (\langle u'w'\rangle^2 + \langle v'w'\rangle^2)^{1/4}$. Note that $u_*(z)$ is the local friction velocity, which is in general different from the value at the ice–water interface, u_{*0}.

2.4. Acoustic Doppler current profiler (ACDP)

A 317 kHz, narrow-band ADCP manufactured by RD Instruments recorded currents from near the ice base (center of first effective bin ≈ 5.5 m) to about 120 m depth. The averaging time interval was varied, being set to either 1 or 2 min. The depth resolution was also varied, being set to either 2 or 4 m. The ADCP was deployed from a frame that was mounted rigidly to the stationary (land-fast) ice, hence no mooring motion correction was required. The beam pairs were oriented with beam 1 pointing approximately southward and beam 3 pointing westward; signals were recorded for each beam. Beam orientation was obtained from observed direction to Gourdeau Point on the southern tip of Lowther Island. This method was preferred to the use of the ADCP's internal compass, since the site was very close to the North magnetic pole. Since the beam-coordinate axes were aligned with the zonal (E/W) and meridional (N/S) axes to within about $3°$, we therefore simply take the zonal and meridional velocities to be $v_x = -v_{34}$ and $v_y = v_{12}$, respectively, where v_{12} and v_{34} are the two horizontal velocity components in beam coordinates (according to the manufacturer's terminology). Root-mean-square (rms) values of the error velocity, v_{err}, varied from about 0.4 to 1.0 cm s^{-1} as the time and depth intervals used for averaging were altered. The ADCP also recorded acoustic backscatter intensity. For the present study, these data were used only to identify unusual, non-passive acoustic targets (e.g., fish and seals) that can corrupt flow field estimates, however they also provide some information on the higher-frequency vertical displacement of reflectors that are assumed to approximately track isopycnals.

2.5. Temperature-salinity mooring

Three Seabird SBE temperature–conductivity (T–C) sensors and eight Alpha-Omega miniature data recorder (MDR) temperature sensors were installed on a 3/16″ kevlar cable, which was moored to the ice and held taut with a 25 kg anchor weight. The thermistors were calibrated in December 1994 at Oregon State University. We used a well-stirred temperature bath in which T drifted at about $2 \times 10^{-3}°$C/min^{-1} over a calibration range of $-2.5°$C to $2°$C. Absolute temperature was provided by a Seabird standard (SBE-544) which is frequently recalibrated by Seabird Electronics in Seattle and is known to have low drift characteristics. The Seacat T–C sensors
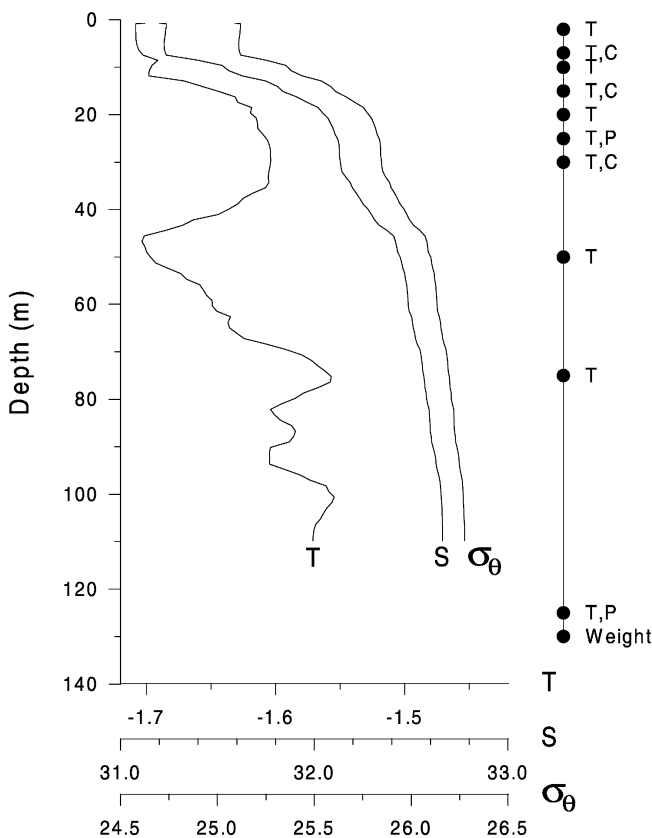
Fig. 4. A typical RSVP hydrographic profile (taken at $t = 125.25$), showing temperature, salinity and density (as σ_θ). Depths of moored MDR (T) and SeaCat CTD (T, C) sensors are indicated. Two of the MDRs also contained pressure (P) sensors. A 25 kg anchor weight was attached to the bottom of the line.

(including SBE-544) were calibrated by Seabird Electronics in March 1994. Instrument noise levels were estimated from spectral analysis of the field data as discussed by Crawford and Padman (1997); typical *rms* noise values for T and S were 3×10^{-3}°C and 7×10^{-3}, respectively. Two of the MDRs also measured pressure (P), at 25 and 125 m.

The instruments were located from 2 to 125 m below the ice base, with the closest vertical sensor separations near the surface where stratification was strongest (Fig. 4). Each sensor recorded 1 sample per minute. The mooring was fully deployed around 23:30 UT, 26 April 1995 ($t = 116.9792$) and recovered around 15:00 UT, 18 May, 1995 ($t = 138.625$). Good data were obtained from all but one of the temperature sensors (MDR-107, at 100 m). The weight at the bottom of the mooring prevented any measurable motion of the mooring line (monitored by the two P sensors) during the entire experiment.

3. Determining vertical diffusivities

Within the SML, when the surface buoyancy flux can be neglected (as during RES95), vertical diffusion is accomplished primarily by the turbulent eddies resulting from the applied stress at the upper boundary: in the present case this stress is provided by the ocean currents relative to the land-fast ice. Within the pycnocline in ice-covered seas, the two main processes that are believed to determine the diapycnal fluxes are shear-driven instabilities and double-diffusive convection (Padman, 1995; Robertson et al., 1995). Because the thermal gradients throughout the water column during RES95 were so weak compared with the salinity gradients, double-diffusion is not expected to be important. The mechanisms we use for determining diffusivities in each environment are discussed in the following subsections.

3.1. Eddy diffusivity in the surface mixed layer

In the nearly neutral SML, eddy viscosity (K_M) is estimated from the product of the local turbulent scaling velocity (u_*) and a mixing length characterizing the vertical exchange scale (λ) of the dominant turbulent eddies (McPhee and Martinson, 1994; McPhee, 1994). In these studies (see also McPhee and Stanton (1996)), we have found a robust inverse relationship between the wave number (k_{max}) at the peak in the weighted variance spectrum of vertical velocity and λ, thus

$$K_M = u_* \lambda = u_* c_\lambda / k_{max} \qquad (3)$$

where c_λ is an empirical constant, found to be about 0.85 (McPhee, 1994).

Data from these previous projects have also confirmed Reynolds analogy (i.e., that eddy viscosity and diffusivity are similar in high Reynolds number flow) by showing close correspondence between eddy viscosity determined by Eq. (3) and scalar eddy diffusivities relating $\langle w'T' \rangle$ and $\langle w'S' \rangle$ to their respective mean vertical gradients (McPhee and Martinson, 1994; McPhee and Stanton, 1996). We presume here that the relationship similarly holds for the tidally driven boundary layer under fast ice, although measured turbulent heat flux in the SML during the RES95 project was too small ($< 1 \, W \, m^{-2}$) to confirm Reynolds analogy directly.

3.2. Shear instabilities in the pycnocline

Shear instabilities due to internal gravity wave (IW) velocity shear are known to be responsible for much of the diapycnal mixing that occurs away from stress boundaries (Gregg, 1987, 1989). Internal waves are free oscillations in the density stratification, with frequencies ranging from f (the local inertial frequency) to N (the local buoyancy frequency). In the latitude range of the RES95 measurements, f lies within the frequency band occupied by semi-diurnal tidal constituents, about 0.08 cycles per hour (cph). Maximum values of N are about 15–20 cph at the base of the SML. The mechanisms by which IWs can lead to diapycnal fluxes have been described extensively in the literature (e.g., Gregg, 1987) and will not be repeated here. However, a fundamental parameter describing the potential for dynamic instability of a sheared

fluid flow is the gradient Richardson number, Ri, which is given by

$$Ri = \frac{g}{\rho} \frac{\partial \rho/\partial z}{|\partial \boldsymbol{U}/\partial z|^2} = \frac{N^2}{|\partial \boldsymbol{U}/\partial z|^2}, \tag{4}$$

where g is the gravitational acceleration, ρ is the fluid density, and $\boldsymbol{U}(z)$ is the horizontal velocity vector. The development of instabilities that lead to turbulence is associated with low values of measured Ri: depending on the instability type, a critical value of Ri for the onset of turbulence ranges from 0.25 to about unity. The important features of the fluid flow are, therefore, those that change $\partial \rho/\partial z$ ('strain') and those that impose velocity shear.

Fluxes within a turbulent pycnocline can be evaluated using data obtained from microstructure profilers. Again, the details have been reviewed by several authors (e.g., Gregg, 1987; Caldwell and Moum, 1995). The two most common procedures involve resolving the vertical wave number spectrum of the scalar gradient, and resolving the spectrum of the velocity gradient fluctuations. This latter procedure is called the 'dissipation' method. Because the principal stratifying scalar at RES95 is salt, whose vertical wave number spectrum cannot be adequately resolved by the RSVP, we use the dissipation method. The equations are given in the following section, but the reader should refer to Gregg (1987) for further details.

3.3. Eddy diffusivity determined by the dissipation method

By resolving the vertical wave number spectrum of the vertical gradient of u_z, the dissipation rate of turbulent kinetic energy (ε) can be estimated from Eq. (1). We then assume that the buoyancy flux (B_ρ) can be approximated by $B_\rho = \Gamma\varepsilon$, where Γ is called the 'mixing efficiency'. Then the diapycnal 'eddy' diffusivity, K_v, is given by

$$K_v = \frac{\Gamma\varepsilon}{N^2}. \tag{5}$$

This procedure relies on a number of assumptions that can each be challenged. For a wide range of observed oceanic conditions, the isotropy assumption used to obtain Eq. (1) is not valid, and the possible range of Γ is quite large (Moum, 1996). Additional uncertainty is caused by the need to assume that, in a region where density stratification is due to both T and S, both scalars diffuse with the same K_v. Despite these caveats, measured diffusivity based on microstructure profiling in the open ocean has provided estimates of K_v that are remarkably close to values obtained by monitoring the large-scale dispersion of released tracers (Ledwell et al., 1993; Ruddick et al., 1997).

4. Observations

4.1. Hydrographic variability

A typical hydrographic profile from RES95 consisted of a thin SML bounded below by a halocline with a buoyancy frequency of $N \approx 15$–20 cph (Fig. 4). Below this

halocline, N decreased slowly with increasing depth. The temperature profile was complex, with a 'warm' intrusion centered near 30 m being a common feature during much of the experiment. However, the total change in T (denoted ΔT_{tot}) from the surface to 125 m rarely exceeded 0.35°C, while the observed total change in S (ΔS_{tot}) was about 1.5. The depth-averaged 'bulk' density ratio, $\langle R_\rho \rangle = \beta \, \Delta S_{tot} / \alpha \, \Delta T_{tot}$, where β and α are, respectively, the saline contraction and thermal expansion coefficients, was $O(100)$. That is, in a bulk sense, ΔT_{tot} plays almost no role in the total density change with depth. This high value of $\langle R_\rho \rangle$ also supports our contention that double diffusion can be ignored when estimating diapycnal fluxes for this environment.

The mooring data provided the only truly continuous description of the time-dependent hydrographic field during RES95. For present purposes, the mooring data were low-pass filtered using a phase-preserving, net 8th-order Butterworth filter with a cutoff frequency of 1 cph. The dominant signal in $T(t, z)$ (Fig. 5a) is semidiurnal with some superposed diurnal variation. Advection of lateral and vertical gradients by the tidal currents is the most likely cause of this variability. Significant lower-frequency variation also occurred, e.g., the 'warm' pulse in the depth range 15–40 m from DOY 129 to DOY 135. There is also a suggestion of an earlier warm water pulse on DOYs 117 and 118, near the beginning of the mooring record. A time series of S at 15 m (Fig. 5b) also shows semidiurnal variability, and again there was a large low-frequency variation in both 'mean' values and high-frequency variance. Time series of current speed (Fig. 5c) are representative of the SML, $|U(t)|$ (5 m), and the deep water, $|U(t)|$ (73 m). Again we see low frequency variability, with a time scale of about 15 d, close to the spring/neap cycle that results from superposition of M_2 and S_2 tidal constituents. This spring/neap variability is seen in the mean current speed, and also in the frequency content of the speed records.

The depth of the SML, h_{SML}, during the experiment averaged about 7 m (from the RSVP data), although various processes caused the instantaneous value of h_{SML} to vary between zero and 12 m. The mean S, T, and density (shown as σ_θ) in the SML were 31.3, -1.714°C (i.e., very close to the freezing point for this salinity), and 25.2. A small spring/neap variation was observed in the daily averaged surface layer T ($-1.719 - 1.707$°C), S (31.19–31.42) and σ_θ (25.08–25.27).

Below the SML, there was almost always a sharp halocline present. The mean depth of the center of the halocline, $\langle z_h \rangle$, and the standard deviation of this depth, evaluated for each batch of RSVP profiles ($\sigma_{z,h}$), are listed in Table 1. Both of these variables appear to be correlated with the spring/neap cycle in tidal currents: both $\langle z_h \rangle$ and $\sigma_{z,h}$ were largest during spring tides.

Below the sharp halocline, the buoyancy frequency slowly decreases with increasing depth. We denote this depth range as 'deep water'. The time scales of variability in the deep water hydrographic properties are best seen in the plot of $T(t, z)$ (Fig. 5a). As with the SML and the halocline, the deep water temperature varies on tidal and spring/neap time scales.

Temperature–salinity data from two RSVP batches (3 and 8) illustrate the range of mean T–S characteristics experienced during RES95 (Fig. 6). Since there was significant scatter in the data during each of these periods, we plotted the range of observed
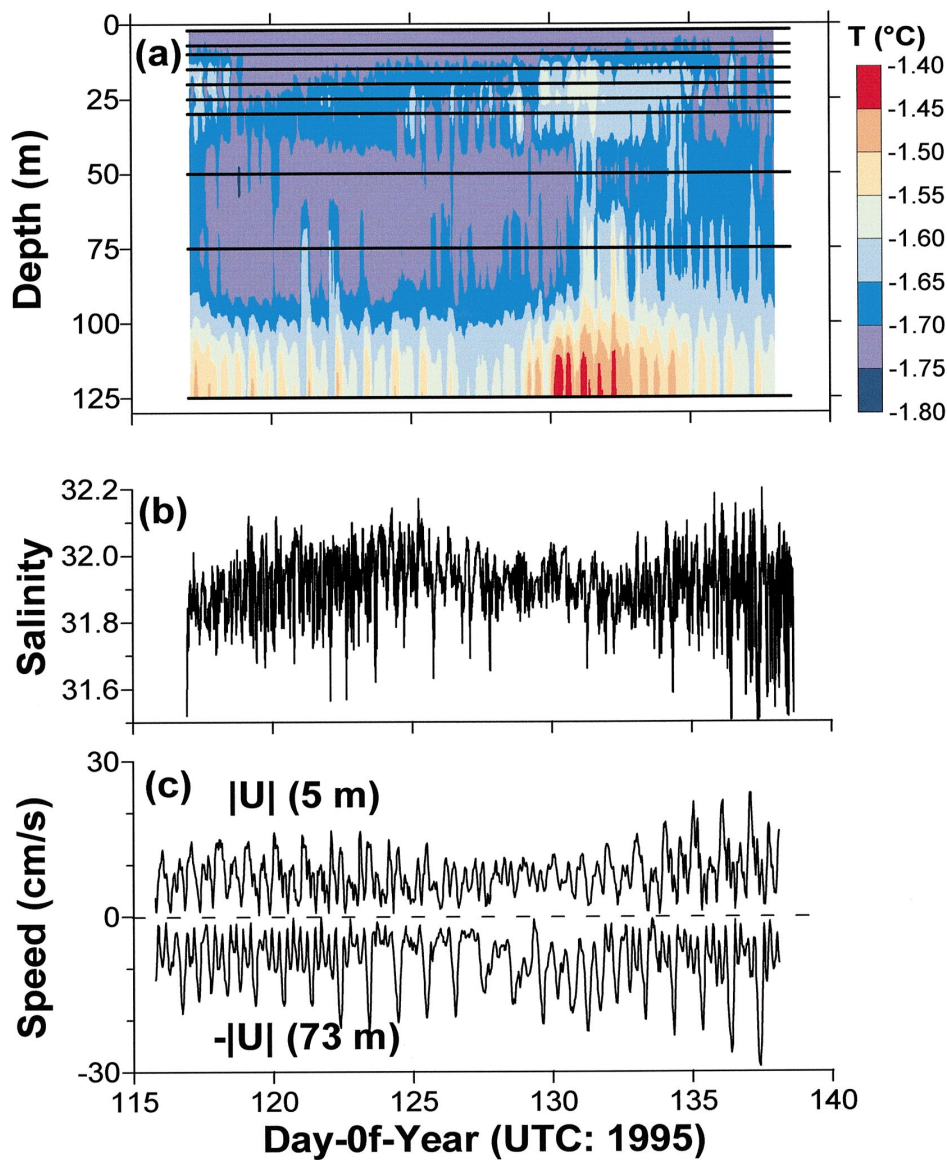
Fig. 5. Time series of (a) moored temperature, $T(t, z)$; (b) salinity, $S(t)$, at 15 m depth; and (c) current speed, $|U(t)|$, at depths of 5 and 73 m. Data have been low-pass filtered as described in the text.
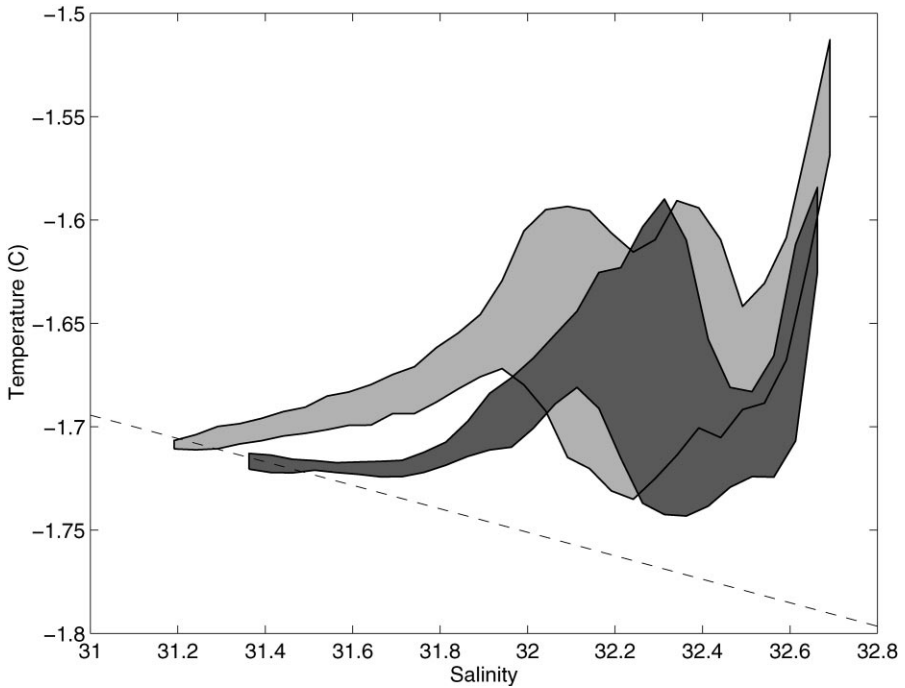
.

Fig. 6. The ranges of temperature and salinity values for RSVP batches 3 (dark) and 8 (light) are shown. The dashed line corresponds to the freezing temperature as a function of salinity for one-atmosphere pressure.

$T–S$ values for each batch. The variability of T for each value of S can be explained by the lateral advection of along-isopycnal property gradients.

Intrusions of warm water similar to those seen in Fig. 5a have been observed in, and just below, the halocline in Barrow Strait during spring by previous investigators. Herlinveaux et al. (1978) found warm water intrusions between about 40 and 80 m, below the base of the sharp halocline at 74°30′N, 91°21′W (near the southwestern tip of Devon Island; their Station BA1) between 19 April and 27 April 1973. Prinsenberg and Bennett (1987) presented hydrographic profiles collected in April 1982 (year-days 88, 94 and 112) a few kilometers south of Cornwallis Island and roughly 10 km east of Resolute (their Station 42). They also described a cold subsurface layer lying between 50 and 100 m depth, which showed little variation in salinity but significant temperature variability. They suggested that the temperature variations may have resulted from different cooling and mixing rates in the polynyas in Penny Strait, where the water mass characteristics are believed to be formed, with further modification as the water flows through McDougall Sound to Station 42. They also showed that an intrusion of warm, slightly more saline water was also present in the middle of the halocline between 25 and 50 m on day 112, 1982, although the cause of this feature is unclear.

Table 2
Comparison of springtime (April/May) salinity and temperature near the 1995 ice camp location for several studies, in the mixed layer (S_{sml} and T_{sml}) and at 100 m depth ($S_{100\,m}$ and $T_{100\,m}$). The 1985 profile measurements were only made to about 80 m, and so were extrapolated linearly to 100 m values

Year	Reference	Data type	S_{sml}	T_{sml} (°C)	$S_{100\,m}$	$T_{100\,m}$ (°C)
1981	Prinsenberg and Bennett (1988)	Interpolated from CTD survey	31.9	− 1.76	33.1	− 1.5
1982	Prinsenberg and Bennett (1987)	Interpolated from CTD survey	32.2	− 1.77	32.9	− 1.5
1983	Prinsenberg and Bennett (1987)	Interpolated from CTD survey	32.4	− 1.76	32.95	− 1.6
1984	Buckingham et al. (1987)	Interpolated from CTD survey	32.5	− 1.78	32.95	− 1.6
1985	Topham et al. (1988)	CTD time series average	32.2	− 1.77	32.9	− 1.7
1995	Present study	RSVP time series average	31.6	− 1.72	32.6	− 1.64

Most previous springtime hydrographic measurements near Lowther Island were obtained from CTD surveys in the early 1980s: these surveys generally consisted of CTD profiles at a variety of locations rather than time series at one location as in RES95. The water column near our site appears to have been fresher in April/May 1995 than during the same season in those previous years (Table 2). This is particularly clear in the SML, which is relatively unaffected by internal waves and the spring-neap modulation (at this time, the SML temperature tends to be at the freezing point, so the lower salinity during RES95 was accompanied by a slightly higher temperature as well). At greater depths, internal wave activity and the presence or absence of 'pulses' described earlier may be responsible for some variability in instantaneous measurements of salinity at depth. Based on our measurements, however, the salinity at 100 m over a spring/neap cycle had a maximum variation of about ± 0.07 and an *rms* value of about 0.02; the 100 m salinity in 1995 is therefore significantly lower (at least 0.3) than the other studies listed in Table 2. The reason for the presence of this relatively fresh water is not understood, nor is its significance to the overall hydrography of Barrow Strait during this period.

4.2. Velocity structure

The velocity structure revealed by the 300 kHz ADCP can be extremely complex. In one day of data close to the spring tidal current maximum (Fig. 7), there was relatively little vertical structure in the east–west component, however the north–south component showed current differences between upper layer and deeper currents of up to 25 cm s^{-1}. Shear during this period was often greater than 0.01 s^{-1} through much of the water column and was particularly strong (up to 0.035 s^{-1}) in the depth range encompassing the halocline and the base of the SML.
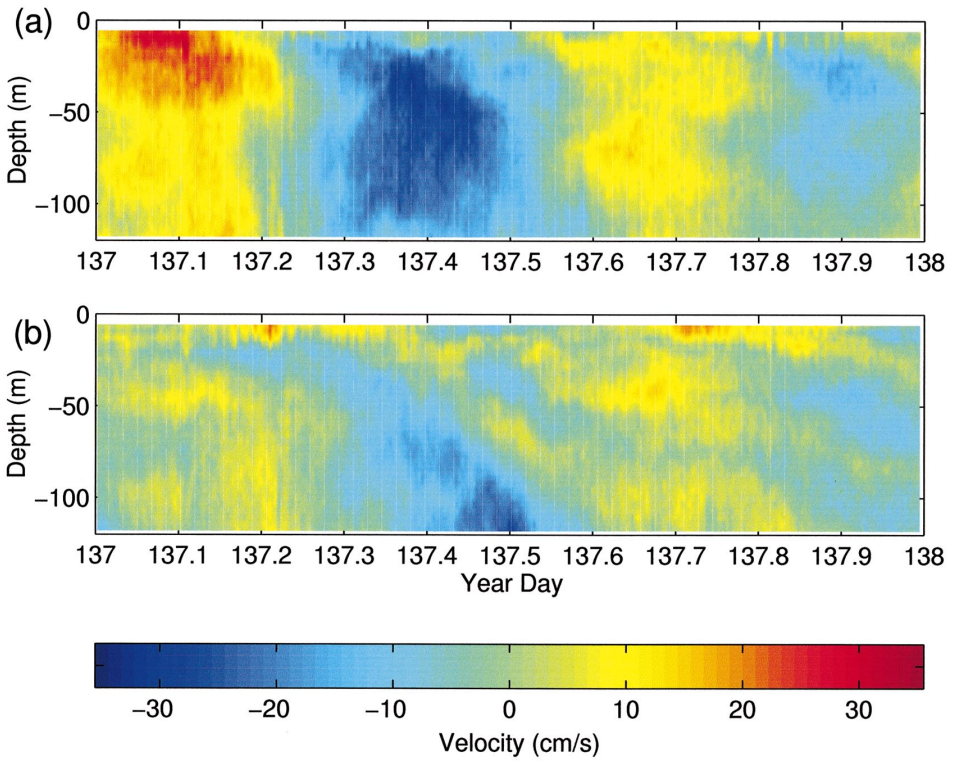
Fig. 7. Horizontal velocity components for $137.0 < t < 138.0$ from the 300 kHz ADCP at Site A: (a) $v_x(t, z)$ (positive east); (b) $v_y(t, z)$ (positive north).
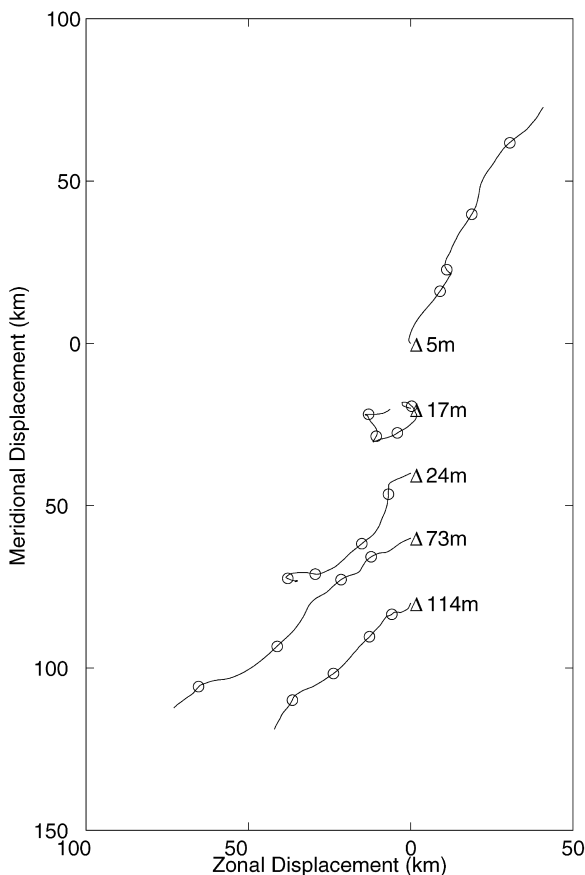
.

Fig. 8. Progressive vector diagrams for the indicated depths: for clarity, paths are staggered by 20 km in the meridional direction. Open triangles indicate the reference position at the beginning of the time series ($t = 115.6875$); successive open circles along the tracks denote the inferred displacements for $t = 120, 125, 130$ and 135.

Progressive vector diagrams for various depths and for the entire period of ADCP observations (Fig. 8) also illustrate the depth dependence of 'mean' flows (i.e., after low-pass filtering the data using a 'tide-killing', phase-preserving, net 4th-order Butterworth filter, with a 48 h cutoff period). There was a mean baroclinic flow, with the thin SML flowing towards the NNE (mean speed ~ 4.3 cm s^{-1}) and the deeper layers moving roughly SW (mean speeds of 3–5 cm s^{-1}). The deepest layers (greater than about 60 m) appear to be strongly constrained by bathymetry, presumably flowing around Lowther Shoal. The low frequency flow at mid-depths (between about 20 and 50 m) showed some variability. The net flow was roughly southward between about DOY 118 and DOY 124, suggesting these waters flowed *between* Lowther Island and Lowther Shoal during this time, while the remainder of the time the flow

was similar to the deeper waters. These observations are consistent with the bathymetry of the region. Lowther Shoal is as shallow as 10 m and thick, multi-year ice can collect near it (Fig. 2), so it is expected to form an effective flow barrier. The channel between Lowther Island and Lowther Shoal is between 50 and 100 m deep, however, so waters at mid-depth are not blocked. The results also suggest that the waters observed just below the halocline in the early part of the mooring record (Fig. 5a) may have originated north or northwest of Lowther Island, while the warm water intrusion at the same depth probably originated northeast of Lowther Shoal.

Tides are the dominant source of current variability. We used least-squares tidal analysis (Foreman, 1993) to determine properties of 18 separate tidal constituents ranging from Z_0 (mean flow) to M_8 (period $\approx$ 3 h). Velocity data were first low-pass filtered (using a phase-preserving, second-order Butterworth filter with a 2 h cutoff period) and subsampled to hourly values before the tidal calculations were performed. Ellipse parameters (Fig. 9) demonstrate that the diurnal current is dominated by K_1, is nearly barotropic, and has high ellipticity (5–10): for depths less than about 100 m, the diurnal tide advects water parcels roughly east and west. The semidiurnal tide, which is dominated by M_2, shows greater variation with depth and lower ellipticities (typically 2–5). The rotation direction changes from counterclockwise close to the surface to clockwise just below the halocline, and back to clockwise at depths greater than about 35 m. This phenomenon has been observed before at high latitudes where the inertial frequency is close to the M_2 frequency (Prinsenberg and Bennett, 1989b; Nøst, 1994): at our ice camp ($\lambda = 74°27.398'$N), $f = 8.029 \times 10^{-2}$ cph and $\omega(M_2) = 8.051 \times 10^{-2}$ cph. In our data set, however, the clockwise term for M_2 dominates over only a short depth range just below the halocline (from about 13–25 m). The observations are consistent with Prinsenberg and Bennett (1989b), who used a simple analytical model to show how different rotary components of the tides are influenced by boundary layer friction. In particular, they showed that when $f \approx \omega(M_2)$, negative rotation of the M_2 tide peaks sharply at the halocline and thus is most influential in that region, while positive rotation is nearly barotropic and hence dominates in the rest of the water column.

Parameters from the tidal analyses were used to reconstruct hourly tidal velocities. Comparisons of the reconstructed velocities to the low-pass-filtered velocities (e.g., Fig. 10a) show some significant differences in the two signals. Spectral analyses of the differences between the two data sets (e.g., Fig. 10b) show significant residual energy in both the semidiurnal band ($\sim$0.08 cph) and in the 4–8 h bands, while residual energy in the diurnal band is fairly low. We interpret these results to indicate that the baroclinic component of the flow is not stationary during the observation interval, while the barotropic flow (including the diurnal band) remains fairly stationary. The inability of the tidal analyses to adequately capture the tidal energy is even more obvious in comparisons of shear, which is our principal concern since it is assumed to be the primary initiator of turbulence in the pycnocline. Fig. 10c compares the time series of shear-squared (S^2) estimates obtained from the low-pass-filtered velocities with S^2 from velocities reconstructed from the tidal analyses. Velocities are first-differenced over a vertical spacing of 3.75 m, and shown here for a central depth of
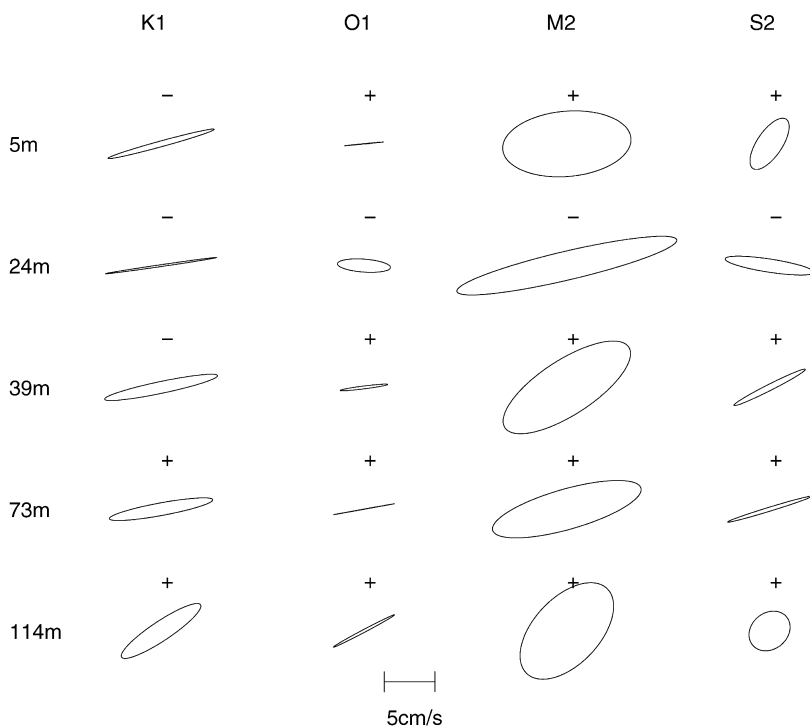
Fig. 9. Tidal ellipses for four major constituents (K_1, O_1, M_2, and S_2) at five representative depths (5, 24, 39, 73, and 114 m). Positive signs indicate that the current vector rotates counterclockwise; negative signs indicate clockwise rotation. Standard orientation is used (north is up, east is to the right).

26.15 m. Shear-squared inferred from tidal analyses typically underestimates the low-pass-filtered S^2 by a factor of 2–3; on time scales of a few hours, the difference in S^2 between the methods can be as high as 2 orders of magnitude. The area-preserving spectrum of the residual S^2 (Fig. 10d) confirms that the shear that is not captured by the tidal analyses is predominantly in the frequency range corresponding to periods of 4–12 h, i.e., the band occupied by semidiurnal and higher-frequency tides. We choose, therefore, to interpret the low-pass-filtered data rather than the reconstructed velocities as the total (barotropic plus baroclinic) 'tidal' flow.

Energetic internal waves were also present. Fig. 11 presents a time series of horizontal kinetic energy density derived from high-pass filtered horizontal velocities and integrated from the surface down to 52 m,

$$KE = \int_{52\,m}^{0\,m} \rho(z)\, \frac{u_{hp}^2(z) + v_{hp}^2(z)}{2}\, dz, \tag{6}$$

where the subscript 'hp' denotes a high-pass filtered component. Here we have used a net 6th-order, phase-preserving highpass Butterworth filter (half-power point at 1 h; 10% at 2 h) on the raw velocity data to mimic the analyses of Marsden et al. (1994a, b).
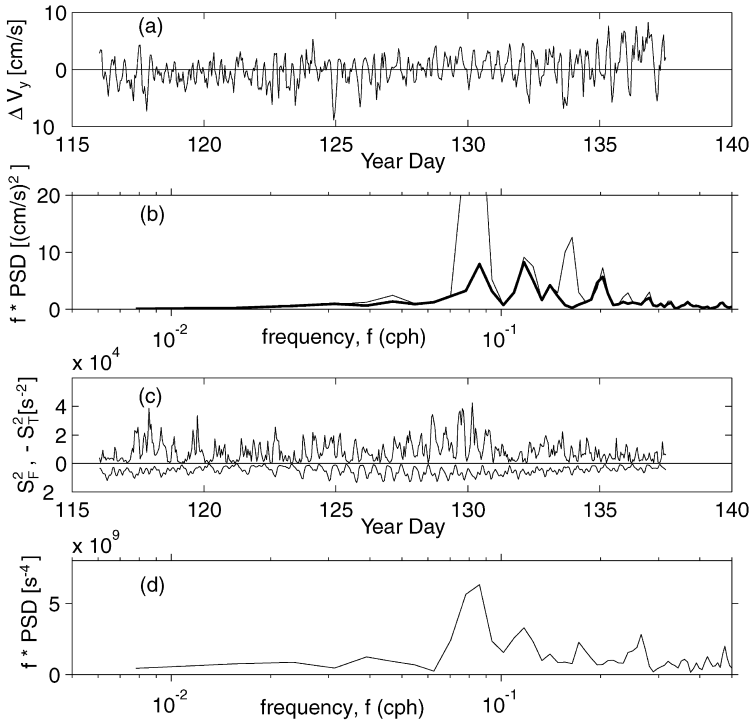
Fig. 10. (a) Time series of the difference between low-pass filtered meridional velocities (v_y) and reconstructed meridional velocities from tidal analysis for the 24.3 m ADCP depth bin. (b) Variance-preserving average power spectra (128 Fourier components) of the low-passed (thin line) meridional velocity and residual (i.e., low-pass filtered minus reconstructed (thick line)) meridional velocity for the 24.3 m depth bin. (c) Shear-squared values, calculated over a 3.75 m interval using velocities from the 24.3 and 28 m depth bins. The positive values (S_F^2) are derived from the low-pass filtered velocities; the negative values ($-S_T^2$) represent the negative value of estimates derived from the reconstructed velocities from the tidal analysis. (d) Area-preserving spectrum of the residual shear-squared, S^2 (i.e., $S^2 = S_F^2 - S_T^2$).

The 'spikes' in Fig. 11 identify packets of internal waves which typically appear as three or four wavelets with inherent periods of about 15–20 min. The spikes have a clear spring-neap variation, similar to measurements reported by Marsden et al. (1994a) from nearby Resolute Passage in 1992 (their Fig. 8). These authors also observed a marked spring-neap variation in internal wave activity, although with somewhat higher maximal energy densities (~ 200–300 J m^{-2}, compared with our observations of ~ 100–200 J m^{-2}). Additionally, while their observations show a mixture of linear and non-linear, soliton-like internal waves, ours are generally more consistent with linear waves.

4.3. Eddy diffusivity in the surface mixed layer

Data from turbulence instrument clusters TIC-1 (2 m) and TIC-2 (5 m) below the ice at the Turbulence Frame site (Fig. 3) were organized into 15 min flow realizations
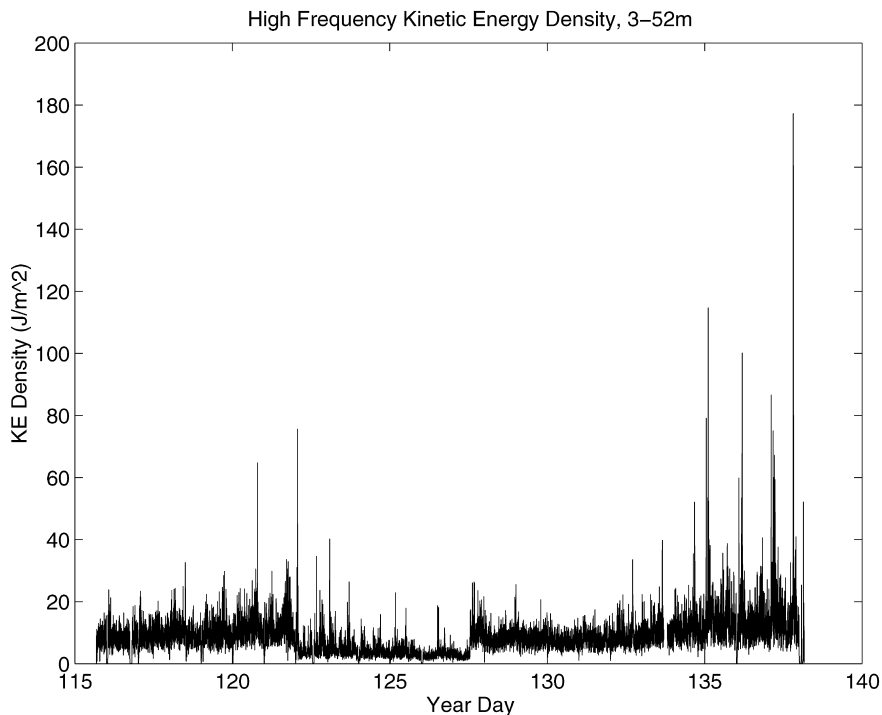
Fig. 11. Horizontal kinetic energy density associated with high-passed horizontal velocities, calculated from 52 m depth to the surface using Eq. (6). The lower 'noise floor' from $t \approx 122$ to $t \approx 127.5$ is due to our choice of different ADCP settings for this period.

as discussed in Section 2.3. Reynolds stress and kinematic heat flux ($\langle w'T' \rangle$) were calculated for each segment, along with vertical velocity variance spectra. Each spectrum was averaged in equispaced logarithmic wave number bins following the method described by McPhee (1994), where wave number (k) is angular frequency divided by mean current speed. Each sample spectrum was then smoothed by fitting (with a high-order polynomial) the averaged spectral estimates multiplied by k. The maximum of the fitted curve was used as k_{max}. Thus the spectrum of vertical velocity for each 15 min realization furnished an estimate of mixing length (λ).

For an overview of eddy diffusivity in the SML, the 15 min data from TIC-1 and TIC-2 were classified by bin-averaged local friction velocity ($u_*(z)$) and λ as functions of mean current speed $U(z)$. Compared with most previous studies of turbulent shear flow under sea ice, these observations (Fig. 12) are distinguished by several features. Data from TIC-1 imply that at higher current speeds, the ice undersurface was hydraulically smooth. At $|z| = 2$ m, we expect a logarithmic velocity profile with the non-dimensional current speed obeying the 'law of the wall',

$$\frac{U}{u_{*0}} = \frac{1}{\kappa} \log\left(\frac{|z|}{z_0}\right),$$

(7)

where u_{*0} is the friction velocity at the interface ($z = 0$), κ is von Karman's constant (0.41), and z_0 is the surface roughness length. The last is usually treated as an independent property of the hydraulically rough surface and varies widely for sea ice, with values as high as 0.1 m reported (McPhee, 1990). If, on the other hand, the surface is hydraulically smooth, the law of the wall depends on the turbulent Reynolds number rather than the explicit surface characteristics, and may be expressed, e.g. (Hinze, 1972) as

$$\frac{U}{u_{*0}} = \frac{1}{\kappa} \log \frac{u_{*0}|z|}{v} + C \tag{8}$$

where v is the kinematic molecular viscosity. Using Hinze's suggested value for C (4.9), z_0 for a smooth surface is $z_{0s} = (v/u_{*0})e^{-2}$. Assuming that Reynolds stress falls off approximately linearly from its surface value to near zero in the upper pycnocline about 10 m from the interface, $u_*(z = 2)$ is about $0.9u_{*0}$, and relationship (8) is plotted as the dashed curve in the upper left panel of Fig. 12. At higher mean speeds, the correspondence is quite close, with derived values of z_{0s} from Eq. (7) in the range $3–5 \times 10^{-5}$ m. This is very small. However, the drag coefficient under fast ice reported by Langleben (1982), also from measurements in the Barrow Strait region, implies a similarly small value for z_0 (McPhee, 1990). Note that since z_{0s} depends on friction velocity, the ratio u_*/U is not exactly linear. Nevertheless, its curvature cannot account for the gentle slope in the data: the roughness appears to decrease with increasing average current speed.

Turbulent mixing lengths based on peaks in the weighted w-spectrum at 2 m (center left panel of Fig. 12) are not inconsistent with surface layer scaling, $\lambda = \kappa|z|$, given the large scatter in the data. There appears, however, to be a downward trend with increasing velocity which, combined with the less than expected slope in the u_*/U ratio, produces eddy viscosity (bottom left panel) nearly independent of flow velocity. For a hydraulically smooth log layer, a monotonic increase in K_M (Eq. (3)) would be expected as indicated by the dashed curve. At higher speeds, the simple approach works reasonably well.

Similar calculations for TIC-2 are shown in the right-hand panels of Fig. 12. Again, at higher current speeds, the surface appears to be hydraulically smooth (assuming that the 5 m Reynolds stress is half the surface value). The ratio, u_*/U is even less linear than for TIC-1: for speeds between 10 and 20 cm s^{-1}, friction velocity is a poor predictor of current speed and vice versa. Mixing length generally increases with increasing speed, but again scatter in the individual spectral estimates is quite large, especially at higher speeds. In contrast to the shallower level, eddy viscosity obtained by combining u_* and λ demonstrates a nearly linear increase with current speed, at approximately twice the slope that would be expected for the idealized log layer (heavy dashed curve). The increase results less from higher friction velocity than from increased mixing length, which also reaches values about twice as large as neutral surface layer theory would predict. Thus, despite the fact that the relationship between stress and velocity near the center of the SML is not straightforward, from a phenomenological viewpoint the eddy viscosity (diffusivity) and current speed are related
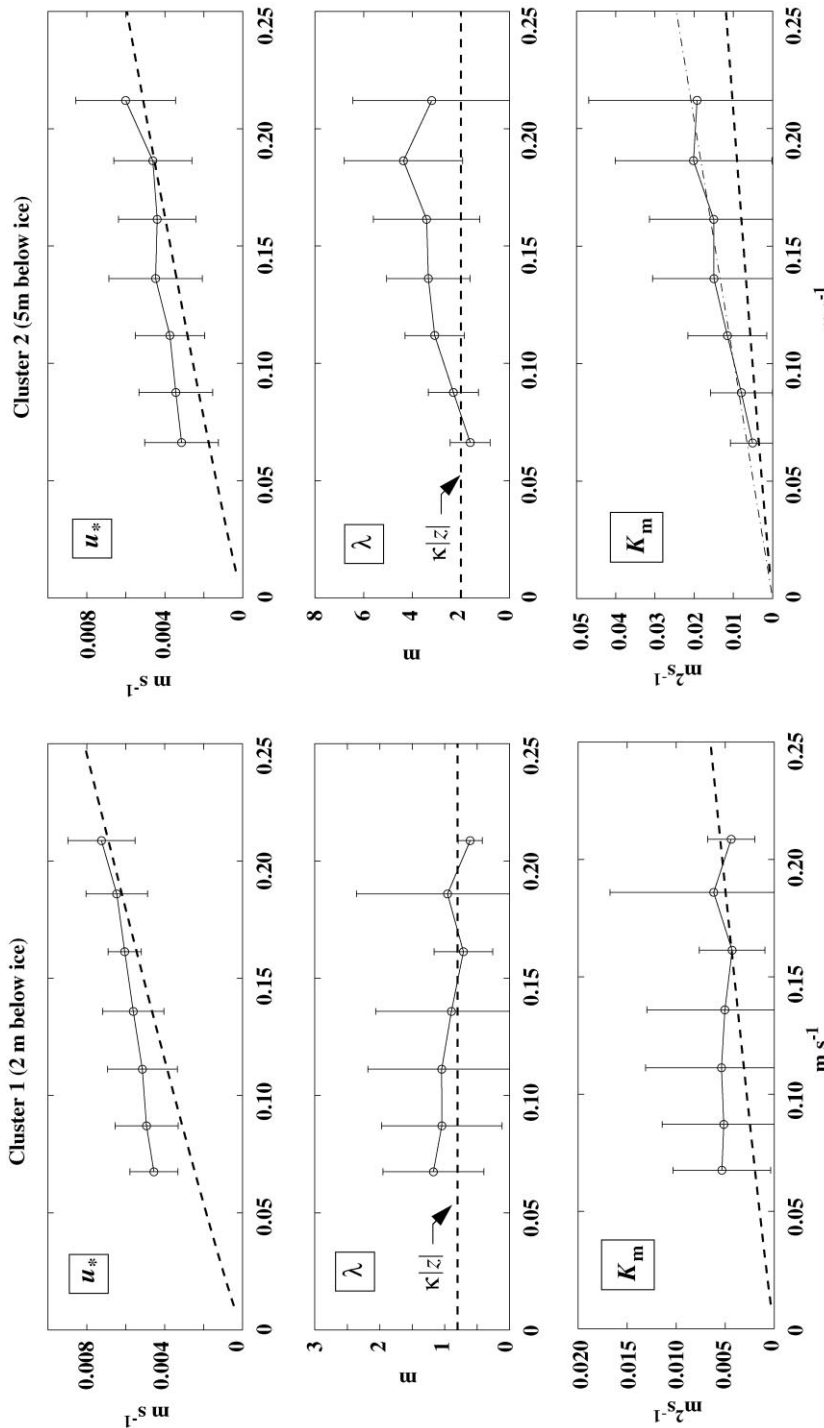
Fig. 12. Friction velocity (u_*), mixing length (λ), and eddy viscosity (K_M) as functions of current speed ($|U|$) averaged in 2.5 cm s^{-1} bins for TIC 1 (left panels) and TIC 2 (right panels). Error bars for u_* and λ are $\pm$ one sample standard deviation (σ) of the 15 min samples in each bin. For K_M, $\sigma = \sigma_{u*} \bar{\lambda} + \sigma_{\lambda} \bar{u}_*$. In each case, the heavy dashed lines are the predictions from a simple logarithmic layer model in which the surface is assumed to be hydraulically smooth (Eq. (7)). Reynolds stress is assumed to fall linearly from its surface value to zero near the top of the pycnocline, and mixing length is von Karman's constant times the distance from the interface. The dot-dashed line in the lower right panel is a least-squares linear regression of K_M against $|U|$.

approximately linearly. A straight line through the origin fitted to the TIC-2 values of $K_M(U)$ yields a slope (with 95% confidence interval), $a = 0.098 \pm 0.026$ m, which is drawn as the dot-dashed line in the lower right panel of Fig. 12.

The lack of clear correspondence between u_* and U at both levels in the SML combined with large scatter in λ (i.e., inverse wave number at the spectral peak) and derived K_M suggests that, even in the well mixed layer, other factors besides current shear influence the turbulence scales and mixing efficiency. In the present analysis, we came across one feature of the flow which indicates asymmetry in the effective drag and eddy viscosity, and may bear on the general problem of evaluating mixing in tidal flows where there is a mean density gradient advected with the tidal ellipse (e.g., an estuarine salt-wedge). In cyclic flow with a horizontal density (salinity) gradient, buoyancy may affect the turbulence scales even when buoyancy flux from melting or freezing at the surface is unimportant, as during RES95. With vigorous vertical mixing, frictional shear near the immobile ice/ocean boundary will cause the magnitude of the tidal ellipse to increase with depth, leading to differential advection of the underlying density field. During the part of the tidal cycle when overall salinity is increasing in the SML, we might thus expect turbulence scales to be suppressed as denser water is advected faster at depth, creating conditions analogous to a stabilizing surface buoyancy flux from melting in a horizontally homogeneous regime. When SML salinity is decreasing, the opposite holds and turbulence may be enhanced, as it would be if surface freezing was occurring.

We do, in fact, see evidence in the RES95 data that advective buoyancy affects SML turbulence. The best example occurred during the spring tide late in the project, for which we considered a 6 h period centered at time 137.1, corresponding to a salinity maximum in the mast data. At TIC 2 (5 m below the ice) the average values for current speed and friction velocity in the three hours before the salinity maximum were $\bar{U} = 20.9$ cm s^{-1} and $\bar{u}_* = 0.56$ cm s^{-1}. Corresponding values for three hours after the maximum were 15.6 and 0.56 cm s^{-1}, respectively. Thus for the same mean stress, the effective drag is considerably higher after the maximum, as would be expected if K_M increased. The asymmetry was observed in several other tidal cycles, and must be at least in part responsible for the 'flattened' u_*/U ratio apparent in Fig. 12. This interpretation is reinforced by Fig. 13a, showing contours of weighted w-spectral density from each 15 min realization as a function of wave number (abscissa) over the 6 h data segment (ordinate). There is a clear shift to lower wave numbers after the salinity peak. Spectra were averaged for three hours before and after the salinity maximum (Fig. 13b) with k_{max} identified for each regime. Average values for λ and K_M were 0.7 m and 41×10^{-4} m^2 s^{-1} prior to the maximum, and 5.1 m and 284×10^{-4} m^2 s^{-1} afterwards. The shift in scales was not this dramatic with every tidal salinity maximum, but the double-peaked versus single-peaked structure of the spectra before and after the salinity maximum was observed regularly. We conjecture that in the double-peaked spectra the stabilizing buoyancy effect and its interaction with the boundary layer shear determines the higher wave number peak, while the geometry of the mixed layer, perhaps interacting with the internal wave field in the underlying halocline, sets the larger scale.
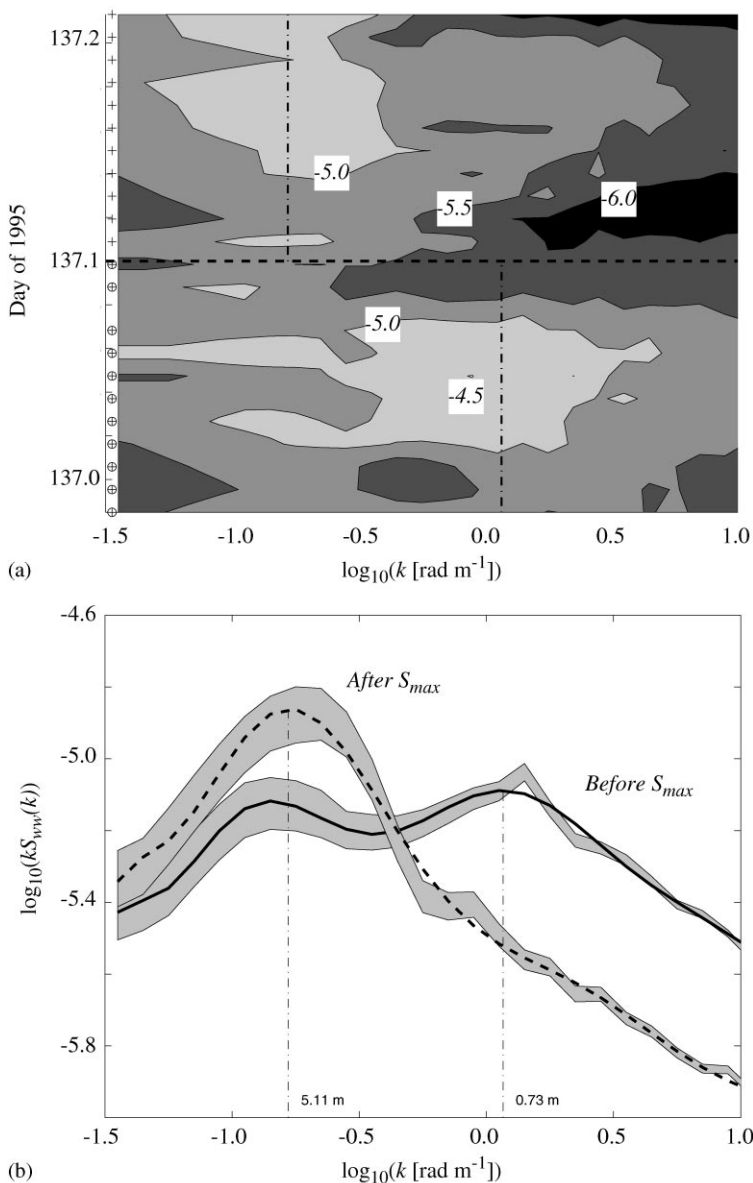
Fig. 13. (a) Contours of $\log(kS_{ww})$ where S_{ww} is the spectral density of vertical velocity variance as a function of angular wave number and time over a 6 h period surrounding the peak salinity value during a tidal cycle (indicated by the horizontal dashed line). Symbols at the left indicate times of the 15 min turbulence samples used to calculate the spectra. (b) Spectra averaged from samples before the salinity and after (identified by open circles and pluses, respectively, in the left margin of (a)), where the shaded envelopes are the 95% confidence intervals for the averaged spectra, and the curves are high-order polynomial fits, used to determine the wave numbers (k_{max}) at the spectral peaks (which are also superposed as vertical dashed lines on the contour plot). Mixing lengths associated with k_{max} values are shown at the bottom of the plot.

4.4. Eddy diffusivity in the halocline and deep water

As a first step towards evaluating and parameterizing mixing in the halocline and deep water, we shall look in detail at the hydrographic, turbulence and current fields for the period corresponding to RSVP batch 9. Fig. 14 presents the time-depth history N^2 (calculated on a 2 m grid), S^2 (calculated on a 3.75 m grid, using the low-pass filtered velocities from Section 4.2), and $\log_{10}(\varepsilon)$. Here we plot from the surface down to 60 m only. Also plotted on each panel in the figure are the depths of the isopycnals, $\sigma_\theta = 25.25$ and $\sigma_\theta = 25.85$, which we use to denote the top and bottom of the halocline. Recall that the temporal separation between consecutive N^2 and ε profiles is typically about 15 min. An exception occurs for the period around day 137.4, when the RSVP was being rapidly cycled through the upper 30 m roughly every 2 min. The 15 min sampling interval is close to the observed background internal wave periods, so internal wave modulations are poorly resolved in the RSVP data and hence in the isopycnal depths.

There are several features to note in Fig. 14. Strong mixing events, identified by enhanced dissipation rates, are present at a variety of depths and times. Large dissipation rates are seen at around 18 m depth near $t = 136.7$, close to the surface near $t = 137.05$, around 45–60 m near $t = 137.1$, and in the middle of the halocline near $t = 135.25$ and $t = 137.4$. The near-surface event near $t = 137.05$ is a particular curiosity: at roughly the same time as the high dissipation rates are observed, the N^2 profile appears to bifurcate, developing a second local maximum near the top of the halocline. One possible interpretation is that the large dissipation rates represent a surface-generated eddy that descends, strips off and entrains a layer of the halocline. This is likely a fairly localized phenomenon, as the buoyancy profiles merge back to a single peak in N^2 by about $t = 137.3$.

We now examine the causes of active mixing by looking in more detail at two turbulence events. We first consider the rapidly sampled halocline event near $t = 137.4$. Fig. 15a shows profiles of N^2 and S^2 in the upper 80 m, averaged between $t = 137.35$ and 137.39 (i.e., 1 h just preceding the start of the halocline mixing event). Here, both N^2 and S^2 are calculated on the same vertical grid (3.75 m spacing) to facilitate interpretation of Ri values. The most significant feature of these plots is that the peak in the shear occurs at a shallower depth than the peak in the buoyancy frequency. The ratio of these two profiles gives the Ri profile; around 15 m depth, Ri is about 0.4, suggesting the potential for active mixing. Indeed, the high dissipation values for this event all occur above the local peak in N^2, where the shear is still high and the buoyancy frequency is much less than the maximum value. This mixing event therefore appears to be a consequence of separation of the location of maximum stratification and maximum shear. The vertical scale of the mixing event is about 10 m. Interestingly, the halocline event around $t = 137.2$–137.25 occurs at a time when the maximal shear is actually *below* the depth of maximum stratification. Again, the vertical scale of mixing is about 10 m. Thus, it would seem that whatever process is responsible for this separation of the stratification and shear fields allows for the creation of low Ri and localized mixing. We note that a larger-scale Ri, calculated across the entire halocline (say 5 to 24 m) gives a value of about 3.5, which would
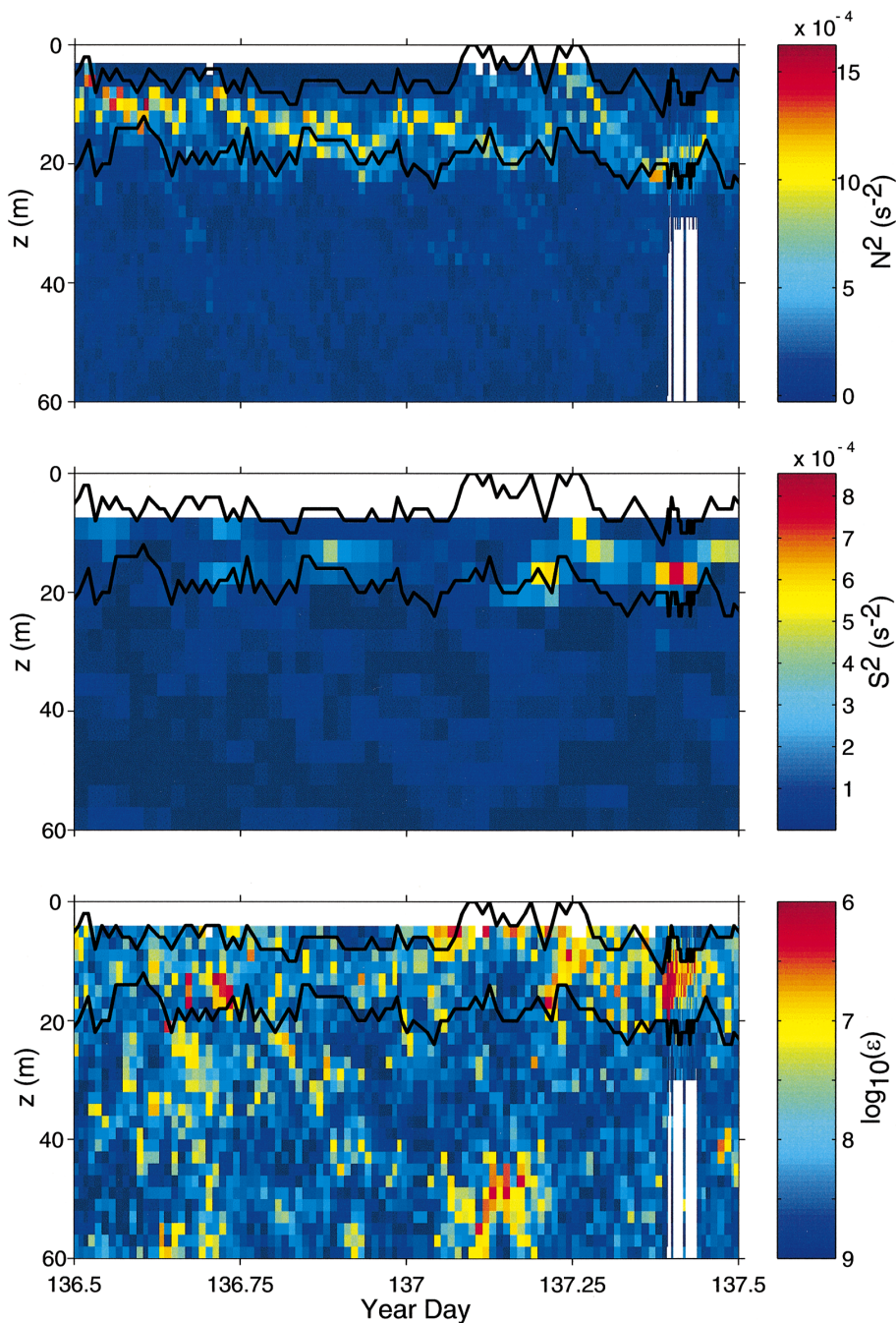
Fig. 14. Stack plot, for $136.5 < t < 137.5$ (RSVP batch 9), of N^2, derived from a 2 m grid of σ_θ (top panel); S^2, derived from a 3.75 m grid of low-pass filtered velocity estimates (middle panel) (see Section 4.2); and $\log_{10}(\varepsilon)$ (bottom panel). Solid black lines in each panel represent isopycnals used to define the top and bottom of the halocline ($\sigma_\theta = 5.25$ and $\sigma_\theta = 25.85$, respectively). Only the top 60 m of data is displayed.
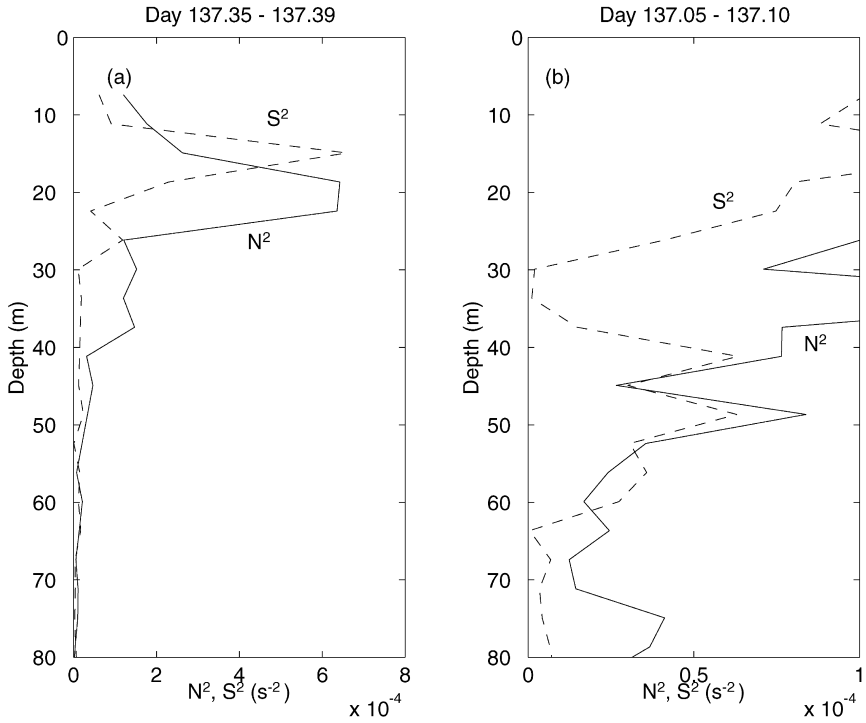
.

Fig. 15. Averaged profiles of N^2 (solid lines) and S^2 (dashed lines) just before mixing events: (a) $t = 137.35$–137.39 (mixing event in the halocline); and (b) $t = 137.05$–137.10 (mixing event between 40 and 60 m).

therefore suggest no instability and no mixing. Consequently, the calculation of such 'bulk' Ri values across the entire halocline is not appropriate for predicting instabilities.

Fig. 15b presents averaged profiles of N^2 and S^2 for the period $t = 137.05$–137.10 (i.e., 1 h preceding the start of the deep water mixing event between $t = 137.1$ and 137.2). The scale has been adjusted to emphasize the relatively high shear between about 40 and 60 m; Ri estimates over this depth range hover around unity and are therefore nearly unstable. Such deep-water mixing events occur over a greater vertical scale than events in the more strongly stratified halocline.

By combining the hydrographic and dissipation rate data from the RSVP, and using Eqs. (1) and (5), we can estimate the diapycnal eddy diffusivity, K_v, in the halocline and deep water as a function of both time and depth during each batch of microstructure profiling. There is some ambiguity, however, as to the most appropriate time and space scales to use for these calculations. By way of example, in individual profiles, N^2 within a mixing patch (or a vertical averaging window for ε) can be quite low, leading to locally large and noisy values of K_v from Eq. (5). On the other hand, if mixing is fairly episodic and/or localized (as is often the case here), then

simply averaging ε for too long a period or too great a depth interval can lead to an average activity index, A_T, Eq. (2), below the critical value. The value of K_v will, therefore, be zero, even though the true average over that period may be non-zero. We have, therefore, determined K_v from averages of ε and N^2, where the averaging scales (temporal and/or spatial) were chosen to be the smallest values that produce smooth estimates of K_v. We assume that the value of N^2 that resists the turbulence, and thus is relevant to the average buoyancy flux during a turbulent event, is the 'mean' background N^2 that is determined by non-turbulent processes such as advection and internal wave strain. We also assume that measured values of ε at a specific time and within a given depth range vary stochastically in a way that is not directly related to variations in the local value of N^2.

Acting on these assumptions, our procedure for deducing K_v is to average N^2 at scales that remove the high frequency, high wave number variability due to turbulence, and to average ε over the same scales. In practice, a temporal averaging interval of 1 h and a vertical averaging scale of ~ 8 m typically provide smooth estimates of K_v. In the following discussion, we choose to characterize mixing in the deep water by focusing on the depth range 50–58 m. The depth range for characterizing the halocline was evaluated in two different ways: by using a fixed depth range (5–24 m) encompassing most of the internal wave modulation of the halocline; and by tracking the depths of two isopycnals ($\sigma_\theta = 25.3$ and $\sigma_t = 25.8$) chosen to represent the top and bottom of the halocline. For both the halocline and deep layer, we calculate block averages of N^2, ε, and K_v (denoted N_h^2, ε_h, and $K_{vh} = 0.2\,\varepsilon_h/N_h^2$, respectively), over hour-long time intervals (typically 4 RSVP profiles). For calculation of the hourly averages, values of ε less than the noise floor, $\varepsilon_n = 2 \times 10^{-9}$ m^2 s^{-3}, are set to zero; if the hourly averaged activity index, $A_{Th} = \varepsilon_h/vN_h^2$, is less than 24, K_{vh} is set to zero.

Fig. 16 shows examples of N_h^2, ε_h, and K_{vh} in the halocline and at depth for a spring period (RSVP batch 9). N_h^2 in the halocline was quite steady at about 4×10^{-4} s^{-2}. In the deep layer, N_h^2 varied between about 1×10^{-5} and 1×10^{-4} s^{-2} on a roughly 6 h time scale. Values of ε_h varied substantially in both the halocline (from $\sim 5 \times 10^{-9}$ to 3×10^{-7} m^2 s^{-3}) and at depth ($\sim 2 \times 10^{-9}$ to 8×10^{-8} m^2 s^{-3}). Estimates of K_{vh} also varied greatly, from 0 (values not plotted) to 10^{-4} m^2 s^{-1} in the halocline and from about 10^{-5} to 10^{-3} m^2 s^{-1} in the deep water. In general, the isopycnal tracking technique gave slightly higher halocline values of both N_h^2 and ε_h than the fixed depth technique. However, in calculations of K_{vh} using Eq. (5), the changes in N_h^2 and ε_h tend to cancel each other, so that the halocline diffusivities obtained using the two different methods agree quite well (except at the lowest values: some of the K_{vh} values determined by the isopycnal tracking method go to zero because A_{Th} is too low).

Fig. 17 shows similar plots as Fig. 16 for a neap cycle (batch 5). Results for N_h^2 are similar to Fig. 16, including the low-frequency variability at depth (although the magnitude of fluctuations is reduced by about a factor of 2). Dissipation rates in the halocline were substantially lower during the neap period than during spring. Deep-water values of ε_h are also somewhat smaller, though occasionally comparable to the spring values. Overall, deep-water estimates of K_{vh} were slightly less during neap, while the halocline values of K_{vh} were all zero. In other words, during neap tide, the
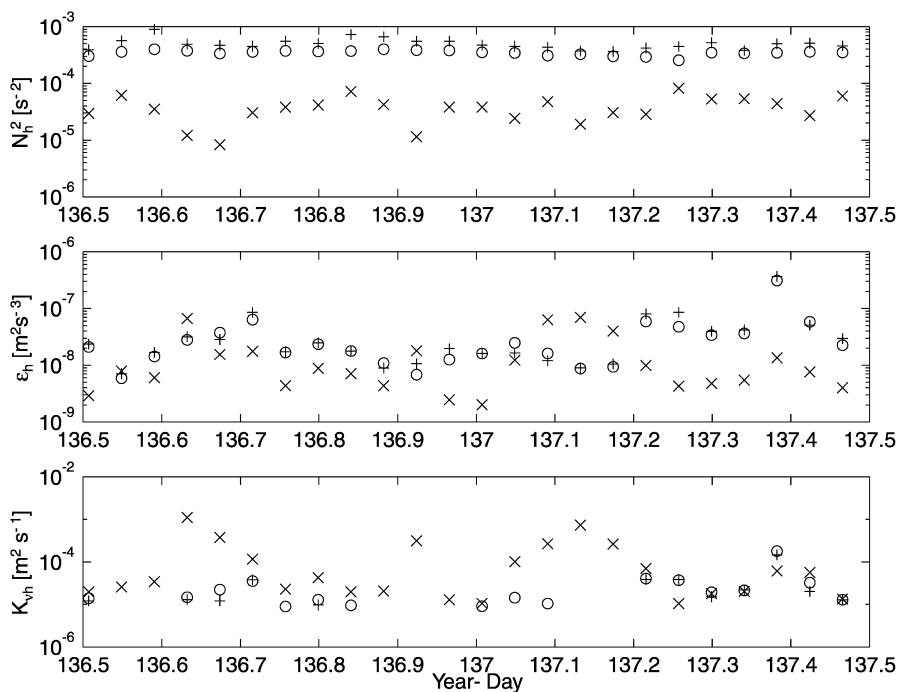
Fig. 16. Time series of (a) N_h^2, (b) ε_h, and (c) K_{vh} for RSVP batch 9 ($t = 136.5$–137.5; spring cycle). Values in the halocline were calculated using an isopycnal tracking method ($\sigma_t = 25.25$ and $\sigma_t = 25.85$; '+') and a fixed depth interval method (5–24 m; 'O'). Deep water values were calculated over a depth interval of 50-58 m ('×'). K_{vh} is set to zero when the hourly averaged activity index (ε_h/N_h^2) is less than 24; these data points are not plotted in (c).

halocline is a very effective barrier to vertical turbulent transport of scalars, isolating the SML from the still-turbulent deep water.

'Daily' estimates were determined by averaging all hourly estimates within each RSVP batch, and are shown in Fig. 18. Over the 18 d period, the batch-averaged value of N^2 (N_b^2) changed very little in both the halocline and at depth. Batch averages of dissipation rate and diffusivity in the halocline showed significant spring-neap variability, with the average diffusivity during neap tide being essentially zero. Halocline diffusivity was substantially higher (by about a factor of 4) in the second spring period ($t \approx 137$) than in the first ($t \approx 121$). The deep-water dissipation rates and diffusivities showed some modest variability, although it is less clearly tied to springs and neaps. However, as with the halocline values, mixing and diffusion at depth was higher during the second of the two spring tides.

5. Discussion and conclusions

For most practical purposes, such as evaluating upward nutrient supply into the SML, it is sufficient to understand how daily averaged mixing rates vary. As we have
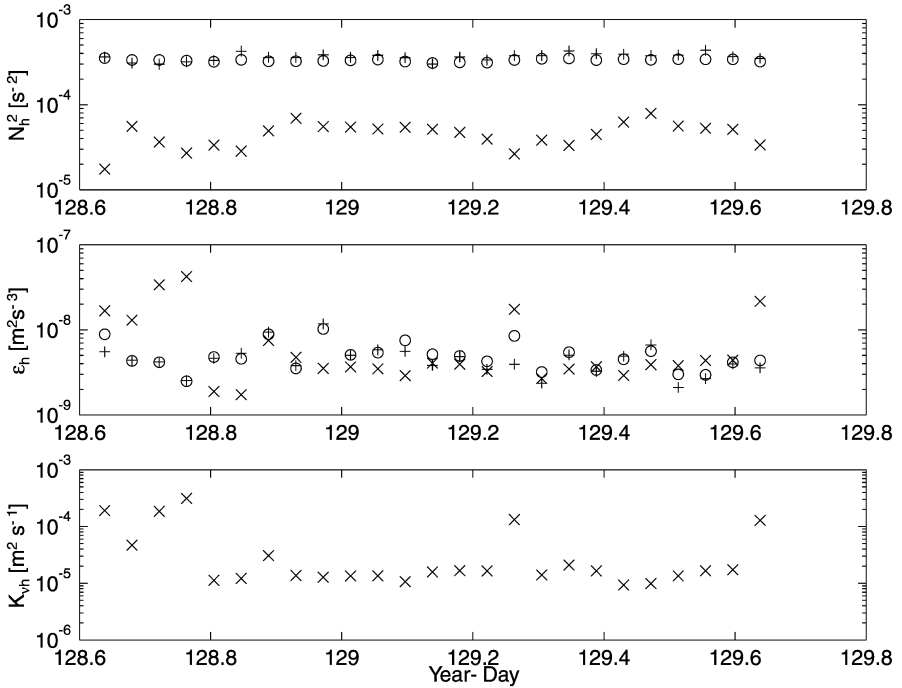
Fig. 17. Same as Fig. 17, but for RSVP batch 5 ($t = 128.6$–129.8). Note that all of the pycnocline values of K_{vh} are zero (off-scale) during this period.

shown, daily averaged hydrographic properties and mixing rates vary with the spring/neap tidal cycle, which has a period of about 15 d. In our RES95 data set, neap tide occurs near $t = 129$ (RSVP Batch 5-6, see Table 1 and Fig. 5b), while spring tides occur near $t = 121$ and $t = 137$ (RSVP batches 1 and 2, and batch 9, respectively). The variation of daily averaged vertical diffusivity, $\langle K_v \rangle$, for the SML, sharp halocline, and deep water ($z \approx 60$ m), are summarized in Table 3. The range of $\langle K_v \rangle$ in the SML is quite small, since it is approximately proportional to the mean value of the SML current speed (see Section 4.3). In the halocline, $\langle K_v \rangle$ varies by an order of magnitude, with a spring tidal value of $\langle K_v \rangle \approx 10^{-5}$ m^2 s^{-1}. The value of $\langle K_v \rangle$ in the deep water varies by about a factor of 3, with a maximum (at the second spring tide) of about 10^{-4} m^2 s^{-1}.

To place these values in context, we note that microstructure measurements in the main oceanic thermocline indicate that the diffusivity due to internal wave shear instabilities is about 10^{-5} m^2 s^{-1} (Gregg, 1989; Ledwell et al., 1993). Higher diffusivities, about 10^{-4} m^2 s^{-1}, are required to satisfy the advection–diffusion balance (Munk, 1966). Several authors have proposed that this order-of-magnitude discrepancy between mid-ocean thermocline measurements and model requirements can be explained by strong mixing at basin edges, including the continental slope (e.g., Armi,
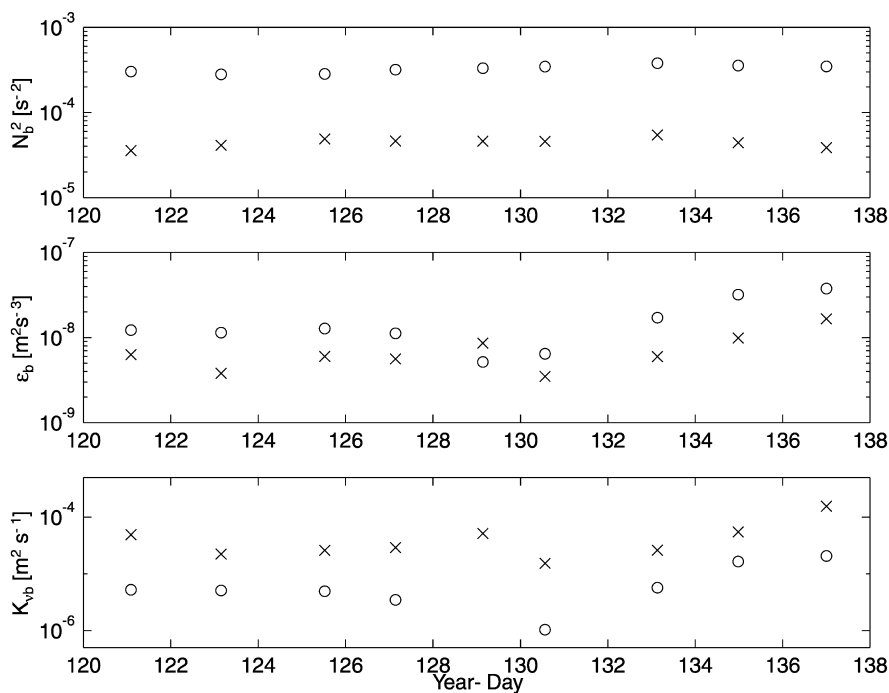
Fig. 18. Batch-averaged time series of (a) N_b^2, (b) ε_b, and (c) K_{vb}. Open circles represent halocline values (5–24 m); crosses represent deep values (50–58 m). The pycnocline value of K_{vb} is zero (off-scale) on day 129.

Table 3
Comparison of daily averaged diffusivity, $\langle K_v \rangle$ ($m^2\,s^{-1}$), for the surface mixed layer, halocline, and deep water, for the two spring tidal periods $t \approx 121$, and $t \approx 137$, and the neap tidal period, $t \approx 129$

Location	Day 121 (first spring)	Day 129 (neap)	Day 137 (second spring)
Surface mixed layer	9×10^{-3}	8×10^{-3}	1.2×10^{-2}
Sharp halocline	8×10^{-6}	8×10^{-7}	1×10^{-5}
Deep water	3×10^{-5}	4×10^{-5}	1×10^{-4}

1978; Wijesekera et al., 1993), over seamounts (e.g., Kunze et al., 1992) and rough topography such as mid-basin ridges (Polzin et al., 1997).

As a summary of the present study, we make the following observations from our measurements during RES95.

(1) On a daily-averaged basis, $\langle K_v \rangle$ in the SML is about $10^{-2}\,m^2\,s^{-1}$: this value is consistent with the first-year, land-fast ice being hydraulically very smooth.

(2) Depth-dependent advection of horizontal density gradients in the SML can change the eddy viscosity by up to a factor of 7. During one-half tidal cycle, this

process acts as an effective surface buoyancy source, then on the other half-cycle, it acts as an effective surface buoyancy sink. This leads to an appreciable asymmetry in surface drag, depending on advection of a horizontal density gradient in the SML shear flow. This may be a common characteristic of, for example, estuarine flows where a horizontal density gradient is carried with the tidal ellipse.

(3) Daily-averaged $\langle K_v \rangle$ in the sharp ($N \approx 15$–20 cph) halocline at the base of the SML varies from $<10^{-6}$ m^2 s^{-1} at neap tide to 10^{-5} m^2 s^{-1} at spring tide. The small values at neap tide indicate that the halocline forms a transport 'barrier' between the deep water and the SML.

(4) In the deep water, daily-averaged $\langle K_v \rangle$ values range from 0.3 to 1×10^{-4} m^2 s^{-1}, however the relationship between $\langle K_v \rangle$ and the spring/neap cycle is not at well defined as for the halocline.

This work corroborates previous studies suggesting that tidal currents are responsible for most of the mixing in the halocline that transports nutrients from the deeper layers in the Archipelago to the surface mixed layer (Cota et al., 1987; Cota and Horne, 1989). The mechanism by which this flux occurs, however, is not primarily turbulence due to stress at the ice–water interface, as previously implicitly assumed. Instead, the most important cause of turbulence is shear across the halocline, which has both a semi-diurnal component (i.e., directly attributable to baroclinic tides) and higher-frequency internal waves that are modulated by changing tidal currents (Marsden et al., 1994a, b). We believe that these waves have been generated by interaction of tidal currents with either the bottom topography or significant under-ice features, for example the land-fast ice to the north of the camp (Fig. 2).

The processes by which tidal energy is ultimately dissipated are extremely complex, as is the distribution of tidal energy within the Archipelago. The present results should not, therefore, be applied indiscriminately to other locations. Nevertheless, this study does identify the processes that would need to be modeled to understand both the physical and biological processes in the Archipelago. The most practical first step for either of these purposes is to develop an accurate, high-resolution, three-dimensional tidal model for the region, possibly with boundary conditions provided by the Arctic tidal model of Kowalik and Proshutinsky (1994) or Lyard (1997).

The observed decrease in salinity in this region between the mid-1980s and 1995 is interesting, although the 8 yr gap between our data and previous observations makes it difficult to assess the cause or evolution of this change. Factors of potential influence include variations in runoff (due to both local and non-local variations in the net precipitation and timing of the freshet) as well as variations in the general circulation of the western Arctic region. Newton and Sotirin (1997) analyzed hydrographic data taken in the Lincoln Sea (northeast of Ellesmere Island) between 1989 and 1994 and determined a general salinity decrease and temperature increase in the upper 80 m or so, with the surface salinity decreasing by about 1.4 over that period. They note that the fresher waters are more indicative of Canadian Basin water, and suggest that the changes were caused by a recent increase in the transport of surface waters from the Canadian Basin into the Eurasian Basin. While it remains to be seen whether or not the changes in the Lincoln Sea are tied to the changes in the Archipelago, the apparent coincidence is intriguing.

Acknowledgements

References

Armi, L., 1978. Some evidence of boundary mixing in the deep ocean. Journal of Geophysical Research 83, 1971–1979.

Baines, P.G., 1986. Internal tides, internal waves, and near-inertial motions. In: Mooers, C.N.K. (Ed.), Baroclinic Processes on Continental Shelves, Coastal and Estuarine Sciences, vol. 3. American Geophysical Union, Washington DC.

Caldwell, D.R., Dillon, T.M., Moum, J.N., 1985. The rapid-sampling vertical profiler: an evaluation. Journal of Atmospheric and Oceanic Technology 2, 615–625.

Caldwell, D.R., Moum, J.N., 1995. Turbulence and mixing in the ocean. Reviews of Geophysics (Suppl. July) 1995, S1385–S1394.

Cota, G.F., Horne, E.P.W., 1989. Physical control of ice algal production. Marine Ecology Progress Series 52, 111–121.

Cota, G.F., Prinsenberg, S.J., Bennett, E.B., Loder, J. W., Lewis, M.R., Anning, J.L., Watson, N.H.F., Harris, L.R., 1987. Nutrient fluxes during extended blooms of Arctic ice algae. Journal of Geophysical Research 92, 1951–1962.

Crawford, G.B., Padman, L., 1997. Physical oceanographic observations from the Resolute 1995 ice camp, Barrow Strait, April/May 1995. Data Report 163, College of Oceanic and Atmospheric Sciences, Oregon State University, Corvallis, OR, 83 pp.

Dillon, T.M., 1984. The energetics of overturning structures: implications for the theory of fossil turbulence. Journal of Physical Oceanography 14, 541–549.

Fissel, D.B., Birch, J.R., Melling, H., Lake, R.A., 1988. Non-tidal flows in the Northwest Passage. Canadian Technical Report of Hydrography and Ocean Sciences No. 98, 143 pp.

Foreman, M.G.G., 1993. Manual for tidal currents analysis and prediction. Pacific Marine Science Report 78-6, Institute of Ocean Sciences, Sidney, B.C., Canada, 66 pp.

Gregg, M.C., 1987. Diapycnal mixing in the thermocline: a review. Journal of Geophysical Research 92, 5249–5286.

Gregg, M.C., 1989. Scaling turbulent dissipation in the thermocline. Journal of Geophysical Research 94, 9686–9698.

Herlinveaux, R.H., Fissel, D.B., Wilson, S.E.G., 1978. Oceanographic observations in Barrow Strait and Wellington Channel, N.W.T., April 1973. Institute of Ocean Sciences, Sidney, B.C., Canada, Pacific Marine Science Report 78-4, 170 pp.

Hinze, J.O., 1972. Turbulence, 2nd ed. McGraw-Hill, New York, 790 pp.

Kowalik, Z., Proshutinsky, A.Y., 1994. The Arctic Ocean tides. In: Johannessen, O., Muench, R.D., Overland, J.E. (Eds.), The Polar Oceans and Their Role in Shaping the Global Environment. The Nansen Centennial Volume, Geophysical Monograph Series, vol. 85. American Geophysical Union, Washington DC.

Kunze, E., Kennelly, M.A., Sanford, T.B., 1992. The depth dependence of shear finestructure off Point Arena and near Pioneer Seamount. Journal of Physical Oceanography 22, 29–41.

Langleben, M.P., 1982. Water drag coefficient of first-year sea ice. Journal of Geophysical Research 87, 573–578.

Ledwell, J.R., Watson, A.J., Law, C.S., 1993. Evidence for slow mixing across the pycnocline from an open-ocean tracer-release experiment. Nature 364, 701–703.

Lyard, F., 1997. The tides in the Arctic Ocean from a finite element model. Journal of Geophysical Research 102, 15,611–15,638.

Marsden, R.F., Paquet, R., Ingram, R.G., 1994a. Currents under the land-fast ice in the Canadian Arctic Archipelago Part 1: vertical velocities. Journal of Marine Research 52, 1017–1036.

Marsden, R.F., Ingram, R.G., Legendre, L., 1994b. Currents under the land-fast ice in the Canadian Arctic Archipelago Part 2: vertical mixing. Journal of Marine Research 52, 1037–1049.

McPhee, M.G., 1990. Small scale processes. In: Smith, W.O. (Ed.), Polar Oceanography. Academic Press, San Diego, CA, pp. 287–334.

McPhee, M.G., 1992. Turbulent heat flux in the upper ocean under sea ice. Journal of Geophysical Research 97, 5365–5379.

McPhee, M.G., 1994. On the turbulent mixing length in the oceanic boundary layer. Journal of Physical Oceanography 24, 2014–2031.

McPhee, M.G., Martinson, D.G., 1994. Turbulent mixing under drifting pack ice in the Weddell Sea. Science 263, 218–221.

McPhee, M.G., Smith, J.D., 1976. Measurements of the turbulent boundary layer under pack ice. Journal of Physical Oceanography 6, 696–711.

McPhee, M.G., Stanton, T.P., 1996. Turbulence in the statically unstable oceanic boundary layer under Arctic leads. Journal of Geophysical Research 101, 6409–6428.

Melling, H., Lake, R.A., Topham, D.R., Fissel, D.B., 1984. Oceanic thermal structure in the western Canadian Arctic. Continental Shelf Research 3, 233–258.

Moum, J.N., 1996. Efficiency of mixing in the main thermocline. Journal of Geophysical Research 101, 12,057–12,069.

Munk, W.H., 1966. Abyssal recipes. Deep-Sea Research 13, 707–730.

Newton, J.L., Sotirin, B.J., 1997. Boundary undercurrent and water mass changes in the Lincoln Sea. Journal of Geophysical Research 102, 3393–3403.

Nøst, E., 1994. Calculating tidal current profiles from vertically integrated models near the critical latitude in the Barents Sea. Journal of Geophysical Research 99(C4), 7885–7901.

Osborn, T.R., Crawford, W.R., 1980. An airfoil probe for measuring turbulent velocity fluctuations in water. In: Dobson, F., Hasse, L., Davis, R. (Eds.), Air Sea Interaction: Instruments and Methods, Plenum Press, New York.

Padman, L., 1995. Small-scale physical processes in the Arctic Ocean. In: Smith, W.O., Grebmeier, J.M. (Eds.), Arctic Oceanography: Marginal Ice Zones and Continental Shelves, Coastal and Estuarine Studies (49), AGU, Washington DC.

Polzin, K.L., Toole, J.M., Ledwell, J.R., Schmitt, R.W., 1997. Spatial variability of turbulent mixing in the abyssal ocean. Science 276, 93–96.

Prinsenberg, S.J., Bennett, E.B., 1987. Mixing and transports in Barrow Strait, the central part of the Northwest Passage. Continental Shelf Research 7, 913–935.

Prinsenberg, S.J., Bennett, E.B., 1989a. Transport between Peel Sound and Barrow Strait in the Canadian Arctic. Continental Shelf Research 9, 427–444.

Prinsenberg, S.J., Bennett, E.B., 1989b. Vertical variations of tidal currents in shallow land fast ice-covered regions. Journal of Physical Oceanography 19, 1268–1278.

Robertson, R.A., Padman, L., Levine, M.D., 1995. Fine structure, microstructure, and vertical mixing processes in the upper ocean in the western Weddell Sea. Journal of Geophysical Research 100, 18,517–18,535.

Ruddick, B.R., Walsh, D., Oakey, N., 1997. Variations in apparent mixing efficiency in the North Atlantic Central Water. Journal of Physical Oceanography 27, 2589–2605.

Rudels, B., 1986. The outflow of polar water through the Arctic Archipelago and oceanographic conditions in Baffin Bay. Polar Research 4, 161–180.

Steele, M., Thomas, D., Rothrock, D., Martin, S., 1996. A simple model study of the Arctic freshwater balance, 1979–1985. Journal of Geophysical Research 101, 20,833–20,848.

Stillinger, D.C., Helland, K.N., Van Atta, C.W., 1983. Experiments on the transition of homogeneous turbulence to internal waves in a stratified fluid. Journal of Fluid Mechanics 131, 91–122.

Stronach, J.A., Helbig, J.A., Salvador, S.S., Melling, H., Lake, R.A., 1987. Tidal elevations and tidal currents in the Northwest Passage. Canadian Technical Report of Hydrography and Ocean Sciences No. 97, 346 pp.

Tennekes, H., Lumley, J.L., 1987. A First Course in Turbulence. MIT Press, Cambridge, MA, 300 pp.

Wijesekera, H.W., Padman, L., Dillon, T.M., Levine, M.D., Paulson, C.A., 1993. The application of internal-wave dissipation models to a region of strong mixing. Journal of Physical Oceanography 23, 269–286.